FACULDADE DE ENGENHARIA DA UNIVERSIDADE DO PORTO

Design of a power harvesting system using TENGs

Ricardo das Neves Esteves

Mestrado Integrado em Engenharia Eletrotécnica e de Computadores

Supervisor: Prof. Cândido Duarte

Second Supervisor: Prof. João Ventura

July 11, 2019

Abstract

With the increase in maritime activities mostly related with research and surveillance of ocean, new ways to supply the power requirements of these technologies have been sought.

The triboelectric nanogenerator (TENG) is an emerging energy harvesting technology that can be used to support the energy needs of small electronic devices. It has been presented as a lost cost, high efficiency and capable of achieving high power densities in a wide range of mechanical sources. Some authors announce that it could also be used in large-scale harvesting, providing a new strategy for wave energy conversion, as an alternative to existent wave farms, based on electromagnetic generators, which are inefficient at low-frequency agitations and bring several technical problems in oceanic conditions.

In this work, it is developed a TENG implementation for harvesting energy from oscillatory movements, like wave oceans, using the triboelectrification effect and electrostatic induction. It is proposed a topology based on freestanding rolling spheres to harvest the energy from low-frequency movements. In a printed circuit board two copper patterns have been designed, which act as electrodes, whereas on top a triboelectric material has been applied. Then, triboelectric materials spheres were placed on PCB, to move freely on the PCB and touching alternately the electrodes, creating a current flow in an external load.

This implementation was tested and optimized under a controlled scenario, finding the parameters that maximize the energy output, and a power management strategy was studied by simulation, to perform the ac to dc conversion and management, enabling the energy storage in an external battery/capacitor.

keywords- Triboelectric nanogenarator, contact electrification, electrostatic induction, ocean energy harvesting, maritime activities

Resumo

Com o aumento das atividades marinhas maioritariamente relacionadas com a pesquisa científica e vigilância dos oceanos, surgiu a necessidade de criar novas fontes de energia que pudessem satisfazer a demanda energética de tais actividades.

Nanogeradores triboeléctricos (TENGs) são uma recente tecnologia que permite produzir energia a partir do movimento, podendo fornecer energia para pequenos dispositivos electrónicos. Esta tecnologia tem-se apresentado como sendo uma solução de baixo-custo, grande eficiência e capaz de alcançar uma elevada densidade de potência para uma grande diversidade de movimentos. Alguns autores anunciam que esta tecnologia poderá ser uma solução para o aproveitamento da energia dos oceanos em grande escala, sendo uma alternativa aos atuais sistemas de produção de energia, baseados em geradores electromagnéticos, que se apresentam como sendo ineficientes a baixas frequências e levantam vários problemas técnicos em condições oceânicas.

Neste trabalho foi desenvolvido uma implementação de um TENG para produzir energia através de um movimento oscilatório, característico da ondulação marítima, usando o efeito triboeléctrico e indução eletrostática. Foi proposta uma tipologia em que esferas de um material triboeléctrico rolam livremente, de modo a captar o movimento de baixa frequência, sobre uma placa de circuito impresso. Nessa placa foram impressos padrões de cobre, que funcionam como eléctrodos, sobre os quais foi despositado um material triboeléctrico. Com o movimento livre das esferas sobre a placa, estas tocam alternadamente nos eléctrodos, criando uma corrente entre os eléctrodos através de uma carga externa.

Esta implementação foi testada e otimizada num cenário controlado, onde foram estudados algumas condições que maximizam a energia produzida. Além disso, uma estratégia de gestão de potência foi estudada por simulação, realizando a conversão ac para dc, de modo a que a energia produzida possa ser armazenada numa unidade externa, como uma bateria/condensador.

Palavras-chave- Nanogerador Triboeléctrico, electrificação por contacto, indução eletrostática, produção de energias a partir das ondas oceânicas, atividades marítimas.

Acknowledgements

First of all, I would like to recognize those who were important for the development of this dissertation project and those that helped me over the past five years, making possible the conclusion of this master degree. I hope that these words could be enough to translate my gratitude.

To my supervisors Prof. Cândido Duarte (FEUP), Prof. João Ventura (FCUP) and to Cátia Rodrigues (FCUP), researcher and PhD student, for their guidance, support, motivation, for the availability every time I needed help and for all the knowledge provided during this last semester.

I have to thank to PhD student Francisco Gonçalves and Vasco Correia of Microelectronic Students' Group (uSG) for all the help, advices and patience whenever some problem occurred.

Also, I want to thank all my colleagues and friends that filled the past five years of amazing memories. In particular to Artur Ribeiro and Miguel Silva, friends that worked near me in the last months. Thankful to have their friendship and support.

Last but not least, I would like to thank to my parents, sister and remaining family, for their love, support and for their sacrifices, giving me the opportunity to continue my studies.

Ricardo das Neves Esteves

"Somewhere, something incredible is waiting to be known."

Carl Sagan

Contents

List of Figures

List of Tables

Abbreviation and Symbols

List of Abbreviations

AUV	Autonomous underwater vehicles
EMG	Electromagnetic generators
FCUP	Faculdade de Ciências da Universidade do Porto
FEUP	Faculdade de Engenharia da Universidade do Porto
PCB	Printed Circuit Board
PDMS	Polydimethylsiloxane
PTFE	Polytetrafluoroethene
TENG	Triboelectric Nanogenerator

Symbols

Q	Charge transferred (C)
V_{OC}	Open-circuit voltage (V)
ε_0	Permittivity of free space (F/m)
P	Power (W)
ε_r	Relative dielectric constant
I_{SC}	Short-circuit current (A)
σ	Surface charge density (C/m^2)
d_1,d_2	dielectric thickness (m)

Chapter 1

Introduction

In line with the vital role of the oceans regarding climate action, environment, and raw materials, maritime activities mostly related with research and surveillance have been increasing in the past years. Species monitoring, deep sea exploration and traffic surveillance in oceans, are some of the activities that have been growing. To satisfy these necessities, several systems have been developed. For example, autonomous underwater vehicles (AUVs) [1,2] covering wide areas in remote oceanic locations, or buoys platforms in the sea, constitute an affordable option to collect essential data about the sea and environmental conditions. These solutions are equipped with a multitude of sensors and electronic systems, powered with their own batteries that need to be charged periodically without human intervention. One solution is the use of solar panels to recharge them. However, normally a solar panel shows a low efficiency and depends on the illumination conditions. The other solution is using energy farms to perform the energy harvest of the dynamics of the ocean, presented mainly in five distinct sources (tidal, water wave, ocean current, temperature and salinity gradient energy), which have been estimated in 75 TW of ocean energy around the world [3,4]. But, these energy farms rely on electromagnetic generators (EMGs), which are inefficient at low-frequency (<5Hz) agitations and bring several technical problems that make these farms an unsatisfactory solution for energy conversion in oceans [5].

The triboelectric nanogenerator (TENG) is an emerging energy harvesting technology that can be used to support the energy needs of maritime activities and ensure the continuous monitoring of environmental parameters in remote oceanic locations or could also be used, in future, in large-scale harvesting providing a new strategy for wave energy. This technology invented recently [5], is currently gaining momentum as a very promising technology, to harvest mechanical energy from various sources, such as mechanical vibration, rotation, wind, human walking and more specifically from water waves and tides [4,6]. The operating principle of a TENG is based on the conjugation of the triboelectric effect and electrostatic induction [4,5], and has been presented as a revolutionary technology due to their very high efficiencies (up to 70 %), high-power densities (above 500 $\mathrm{W/m^2}$), low cost, extreme lightweight and low environmental impacts [4].

1.1 Triboelectric Nanogenerator

Nanogenerator is the technology that can harvest energy from the environment, using nanomaterials and nanotechnology for powering systems. In the last years, a multitude of nanogenerators with diverse applications were created using distinct physical effects, such as: the pyroelectric nanogenerator (thermal effect), the piezoelectric nanogenerator, and the triboelectric nanogenerator.

Nanogenerators based on piezoeletric materials were developed by Zhong Lin Wang and a coworker, to harvest ambient mechanical energy in 2006, opening a new field of energy conversion and application [4]. Then, in 2012, triboelectric nanogenerators based on the triboelectrification effect and electrostatic induction were invented [6, 7]. Fig. 1.1 shows the first TENG presented. In a generic form, a TENG is composed of two materials with different polarities (capacity to gain or lose charges). When these materials are brought into physical contact, electrostatic charges are created on the surface of these materials (triboelectrification) [8]. After that, with their separation by an external force, a potential difference appears, which drives charges to flow between two electrodes attached to each material.

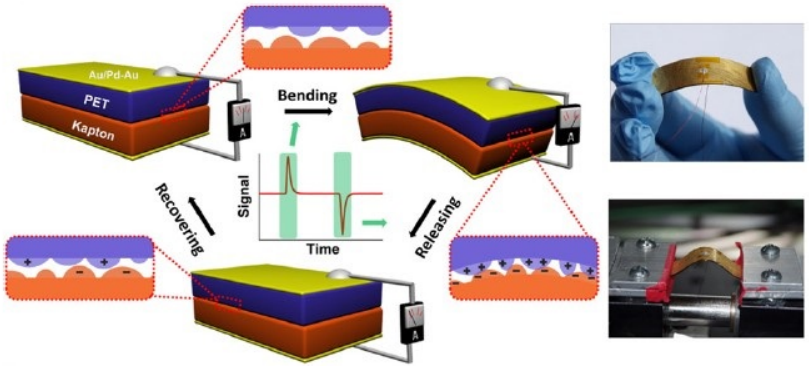

Figure 1.1: First triboelectric proposed in 2012 (from [6]).

1.1.1 TENG designs for blue energy harvesting

The triboelectric nanogenerator has been developed recently because it has been shown as a powerful technology, that could provide an efficient strategy for harvesting wave energy. Different TENG designs for oceanic harvesting energy have been reported in the literature.

The authors of the design depicted in Fig. 1.2 created a duck-shaped structure to efficiently capture the motion of incident waves. The structure contains two copper electrodes covered by a dielectric layer, in which several spheres roll on top, constituting the triboelectric nanogenerator. With 3 units in parallel, an output power density of 1.366 Wm^2 was reported. In Figure 1.3, based on the same working principle, a fully enclosed TENG comprehending a rolling ball inside a rocking spherical shell is proposed, where an output power of 10 mW per unit was achieved.

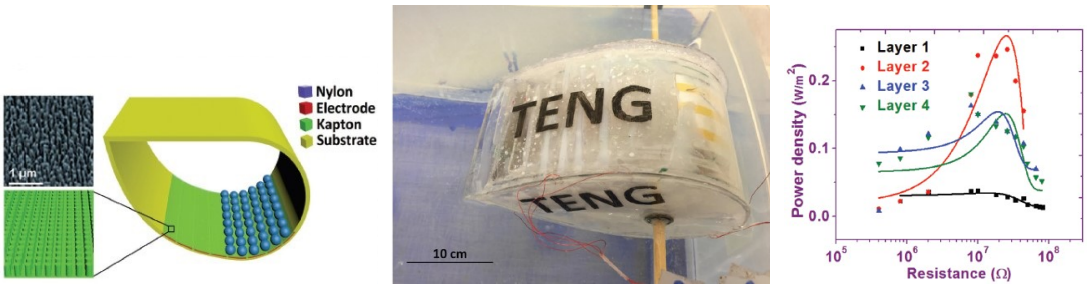

(a) (b) (c)

Figure 1.2: Freestanding duck-shaped energy harvester: (a) Schematic configuration; (b) Photograph of the duck-shaped energy harvester; (c) Output power profile for different number of layers (from [9]).

(a) (b) (c)

Figure 1.3: Fully Enclosed Rolling Spherical Structure TENG: (a) Schematic configuration; (b) Photograph of a rocking nanogenerator floating on water; (c) Power output profile (from [10]).

Alternatively, a tower structure constituting an array of TENGs in an optimized arc surface was presented (depicted in Fig. 1.4), for harvesting wave energy from arbitrary directions. A power density of 1.03 Wm^3 is achieved, increasing linearly with the number of structures attached in parallel.

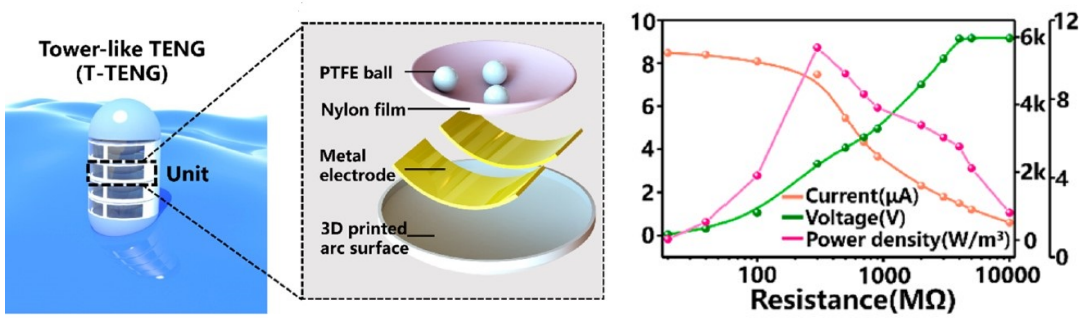

(a) (b)

Figure 1.4: Tower-like Triboelectric Nanogenerator: (a) Schematic diagram; (b) Output power profile with 10 units (from [11]).

A network TENG that consists in a "sandwich" structure is presented in Figure 1.5(b), where repeated TENGs are placed to form a box wall, shown in Figure 1.5(a), with a metal sphere inside that will collide with the TENG units due to wave motion. A network configuration is proposed for large-scale energy harvest. Based on the power output of one unit, it is expected for a network implementation a power output of 1.15 MW for a 1 km^2 surface.

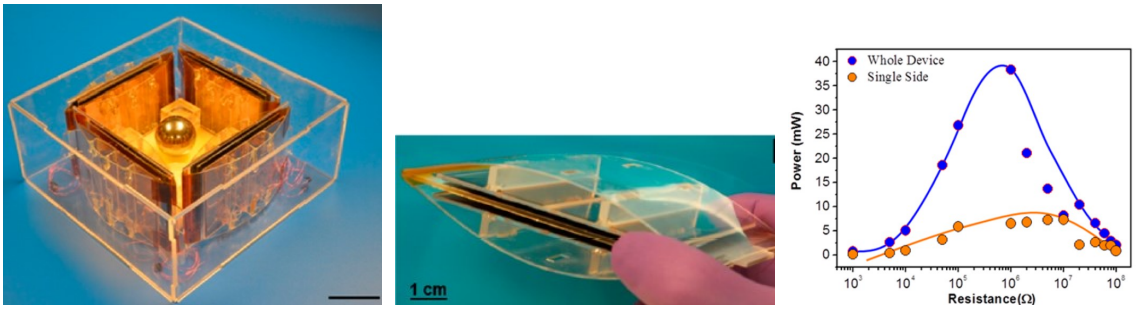

(a) (b) (c)

Figure 1.5: Networks of Triboelectric Nanogenerators: (a) Photograph of implementation; (b) Photograph of the sandwiched structure; (c) Output power profile (from [12]).

1.2 Thesis Objectives

The ultimate goal for a complete TENG implementation in the ocean is to be able to get energy harvesting that could satisfy the power requirements of typical maritime activities, overcoming the drawbacks exhibited by the current solutions, namely in terms of cost and efficiency. As such, this dissertation has the following goals:

- Study TENG-based solutions adequate to power small electronics sensors;
- Experiment different TENG configurations to define a possible structure for ocean energy harvesting;
- Propose a rectifier strategy suitable for the proposed TENG approach.

Due to the novelty of the topic, these goals imply the design and set up of several experimentation structures and testing circuits, so that the tests can be systematic and the required measurements can be obtained.

1.3 Contribution of this work

Some of the experimental results obtained in this work have been presented in a conference during the time frame of the current thesis [13]:

Ricardo Esteves, Cátia Rodrigues, João Ventura, André Pereira, Cândido Duarte, Vasco Correia, and Luís Pessoa. Experimental Evaluation of TENGs for Energy Harvesting in Maritime Applications. In *Proceedings of Oceans 2019, Marseille – Unpublished*. IEEE, June 2019.

1.4 Thesis Organization

This introductory chapter addresses the triboelectric nanogenerator and presents the motivation to develop a system based on it. It also shows some solutions reported in the literature for the energy harvest in an ocean environment.

Chapter 2 addresses the theory of triboelectric nanogenerators, describing the best materials to use, the fundamental modes of a TENG and the flow process that can be used to simulate a TENG.

Chapter 3 presents the several design stages and evolution that lead to the final TENG implementation proposed in this thesis. Furthermore, it describes the fabrication process used in the proposed TENG device.

The next chapters, Chapter 4 and Chapter 5, describes the process chosen to experimentally characterize the TENG: the measuring equipment, results obtained, and the optimization performed to obtain the best power output.

Chapter 6 describes a strategy for improving the energy output and a power management solution for a TENG. All the results presented in this chapter were obtained by simulation.

Finally, Chapter 7 concludes the work and provides future improvements in the work to implement a system for maritime applications.

Chapter 2

Triboelectric nanogenerator

2.1 Triboelectrification effect

Triboelectrification is know for thousands of years and usually attributed to an unwanted consequence of electrostatics in technology or daily life, that can cause damage in our electronic systems, for example.

It is a contact electrification effect in which a material becomes electrically charged after it is contacted with a different material through friction [8]. The mechanism behind triboelectrification is still being studied, however, it is generally believed that after the contact between two different materials, a chemical bond is formed between some parts of the two surfaces, and charges move from one material to the other to equalize their electrochemical potential. The transferred charges can be electrons, ions or molecules [8]. When these materials are separated, the charges previously transferred stay retained in the material for an extended period of time and an electric field is built up, in which the strength of this electric field is proportional to the transferred charges density.

2.2 Materials for Triboelectrification

The materials used have a huge impact on the triboelectrification effect. Although almost every material, such as metals, polymers or wood, suffer of this effect, the ability of a material for gaining/losing electrons depends on its triboelectric polarity [8]. For the greater charge transferred between two materials, the chosen materials should have the most opposite polarities.

Table 2.1, called triboelectric series, shows some conventional materials ordered by their tribopolarities. The materials on the top will attain negative charges when touched with other oppositely charged material and vice-versa. So, the further away two materials are separated from each other in the triboelectric series, the greater will be the charge transferred.

Besides the material, the surface morphology can be modified to improve the charge transference, by enhancing the contact area and possibly the triboelectrification effect. Several physical techniques can be used, like the creation of pyramid-square- or hemisphere-based micro or nanopatterns on the surface of material.

Positive	Polyformaldehyde 1.3-1.4	(continued)	
	Etylcellulose	Polyester (Dacron)	
	Polyamide 11	Polyisobutylene	
	Polyamide 6-6	Polyuretane flexible sponge	
	Melanime formol	Polyethylene Terephthalate	
	Wool, knitted	Polyvinyl butyral	
	Silk, woven	Polychlorobutadiene	
	Aluminum	Natural rubber	
	paper	Polyacrilonitrile	
	Cotton, woven	Acrylonitrile-vinyl chloride	
	Steel	Polybisphenol carbonate	
	Wood	Polychloroether	Negative
	Hard rubber	Polyvinylidine chloride (Saran)	
	Nickel, copper	Polystyrene	
	Sulfur	Polyethylene	
	Brass, silver	Polypropylene	
	Acetate, Rayon	Polyimide (Kapton)	
	Polyvinyl alcohol	Polyvinyl Chloride (PVC)	
	Polymethyl methacrylate (Lucite)	Polydimethylsiloxane (PDMS)	
	(continued)	Polytetrafluoroethylene (PTFE)	

Table 2.1: Triboelectric Series - The tendency of a material lose charges (positive) or gain charges (negative)(adapted from [8]).

2.3 Inherent capacitive behavior and governing equations of a TENG

As referred before, the fundamental working principle of a TENG is a combination of contact electrification and electrostatic induction. Contact electrification provides static polarized charges and electrostatic induction is the mechanism responsible to convert mechanical energy to electricity.

When the two different dielectric materials (tribo-pairs) contacts with each other, the contact surface of the two dielectrics will have opposite static charges (tribo-charges), as a result of triboelectric effect as discussed above. Normally, attached to these dielectric materials are an insulated electrode (Fig. 2.3), in which will be induced charges by the effect of the tribo-charges. As the electrodes are isolated from the dielectrics and in case that they are connected by a external circuit, a charge flow will occur between them to maintain the potential equilibrium (behavior showed in Fig. 2.5). Defining these transferred charge as Q, the charge in each electrode is respectively, Q and -Q.

In any TENG there are mainly two parts that contribute to the electrical potential voltage [6]. The first is the open-circuit voltage ($V_{OC}(x)$) created by the polarized triboelectric charges, which is a function of the separation distance x. The second is the already transferred charge Q on each electrode. The contribution of such charge is -$Q/C(x)$, where C is the capacitance between the

two electrodes, which also is a function of the separation distance. Consequently, the total voltage difference between the electrodes can be given by [14]:

$$V = -Q\frac{1}{C(x)} + V_{oc}(x) \tag{2.1}$$

Eq (2.1), called V-Q-C relationship is the governing equation of any TENGs and represents its capacitive behavior. Under short-circuit (SC), the transferred charges (Qsc) cancel the electrical potential generated from polarized charges, and so, Eq (2.1), under shot-circuit conditions becomes [14]:

$$Q_{SC} = C(x)V_{OC}(X) \tag{2.2}$$

2.3.1 First-order lumped-parameter equivalent circuit model

Based on the two parts that contribute to the electrical potential voltage in EQ (2.1), we can easily derive the lumped parameter equivalent circuit model of a TENG, which can be represented by two circuit elements. The first is originated from the inherent capacitance between the two electrodes, as already discussed, and can be represented by a capacitor. The second is an open-circuit voltage, originated from the separation of the polarized tribo-charge and can be represented by an ideal voltage source (V_{OC}). So, the lumped parameter equivalent circuit model can be represented by a serial connection of an ideal voltage source and a capacitor, as shown in Figure 3.4 [14]. It becomes evident that the inherent impedance of a TENG mainly comes from its inherent capacitance. Due to the high isolation between the two electrodes the internal resistance is almost infinity and so, it is not included.

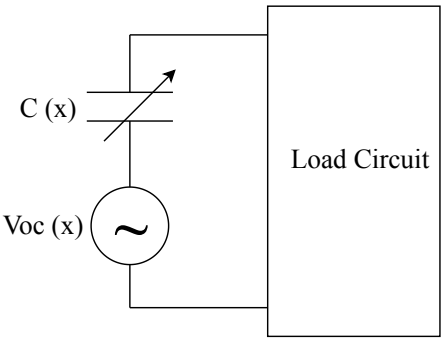

Figure 2.1: First-order lumped-parameter model of any TENG (adapted from [15]).

Based on the circuit model, it is possible to simulate the TENG behavior. Figure 2.2 shows the fundamental simulation method for a TENG, which contains two steps: first the electrostatic simulation and then an electrical simulation.

The electrostatic simulation is realized to find the $V_{OC}(x)$ and $C(x)$ functions in the V-Q-x relationship. This can be done by an analytical derivation, but only works for the simplest configurations. A general method that works for all TENGs is numerical calculation based on finite

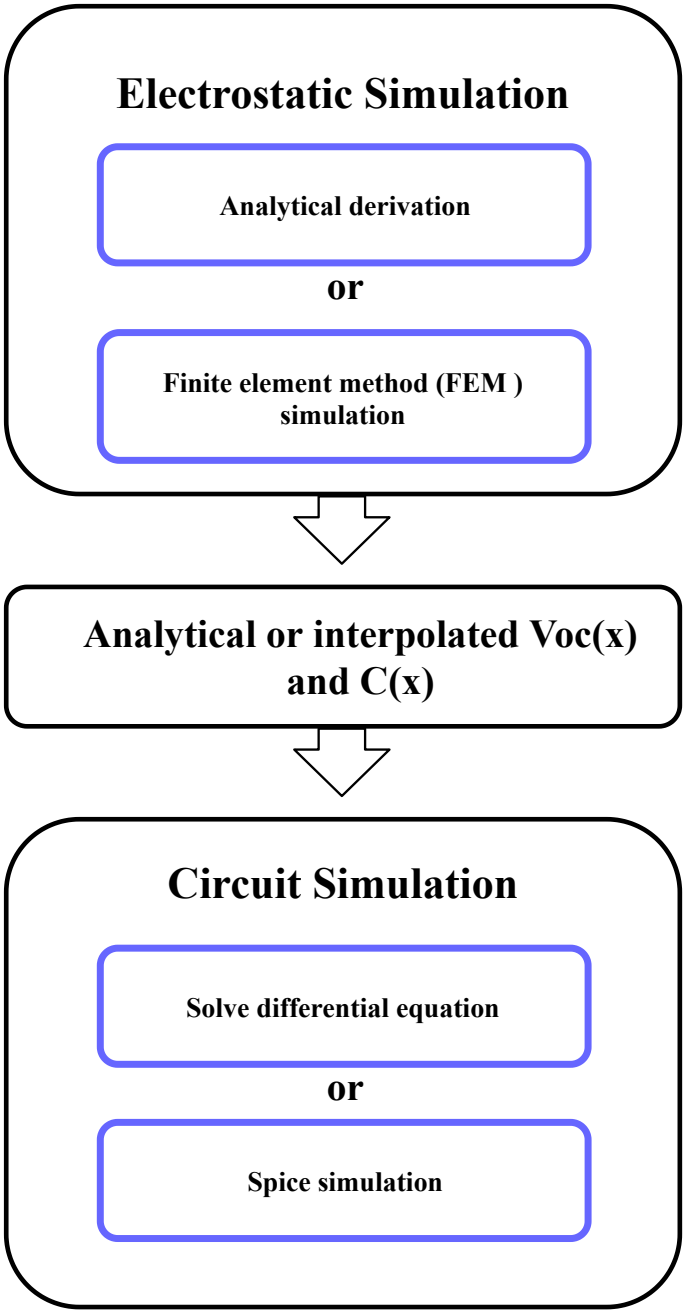

Figure 2.2: Simulation of a TENG (adapted from [8]).

element method (FEM) and can be performed using a FEM simulation software, like COMSOL and ANSYS [14].

After obtaining $V_{OC}(x)$ and $C(x)$, a circuit simulation [15] can be done to obtain the output characteristics, which can be performed by solving a differential equation, such as [15, 16]:

$$R\frac{dQ}{dt} = -\frac{1}{C}Q + V_{OC} \tag{2.3}$$

Figure 2.3 represents a TENG system with a purely resistive load. However, for more complex

loads, solving differential equation can be much more difficult. A general method is using SPICE software to simulate the real-time output characteristics, embedding the circuit model into the software and specifying the initial condition and motion process.

2.4 Fundamental Modes

In this subsection will be presented the four basic configurations of TENG, which will be explained below with focus on the V_{OC} and the C for each different configuration.

2.4.1 Vertical Contact-Separation Mode

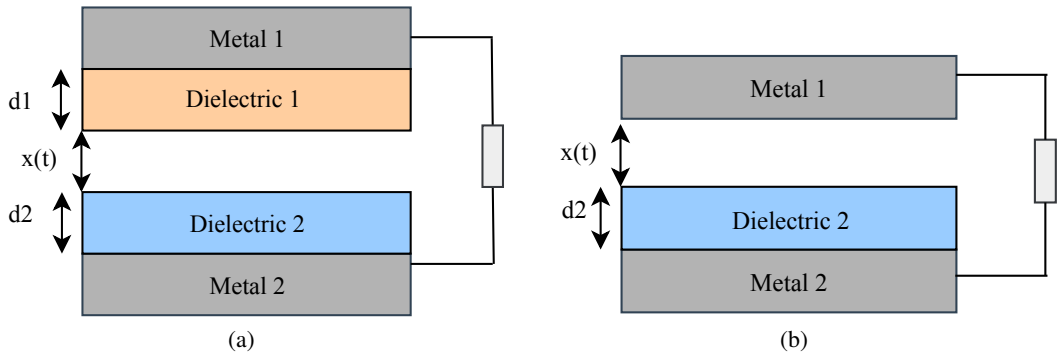

Figure 2.3: Vertical Contact-Separation Mode: (a) Dielectric-to-dielectric and (b) conductor-to-dielectric.

The first developed TENG mode, which can be divided into two categories based on the materials for the triboelectric pairs: dielectric-to-dielectric (Fig.2.3(a)) and conductor-to-dielectric (Fig.2.3(b)).

In a dielectric-to-dielectric, two dielectrics materials (dielectric 1 and dielectric 2) with thickness of d_1 and d_2 and relative dielectric constants of ε_{r1} and ε_{r2}, are placed face to face with a electrode attached, as illustrated in Fig.2.3(a). In a conductor-to-dielectric type (Fig. 2.3(b)), the working mechanism is the same, but now the metal 1 plays two roles because it is now part of both the triboelectric and electrode layer.

Figure 2.4 shows the working principle of this configuration under an open-circuit condition, which under a mechanical force, the distance x between the two materials will vary. In an initial state, there are no charges on the surface of a material and so, no electric potential difference exists between the two electrodes. After the contact, the inner surface of the two dielectrics will have opposite tribo-charges with the same charge density (σ), due to the triboelectric effect (Fig. 2.4(I)), in which the tendency to gain or lose charges of each dielectric, is done according to the triboelectric series, as presented above. Regarding triboelectric materials (insulators) it is reasonable to assume that the tribo-charges are uniformly distributed at the two surfaces with negligible decay [8].

When the applied force is removed and the distance between materials starts to increase, a potential difference between the two electrodes is induced (Fig. 2.4(II)), until the maximum distance

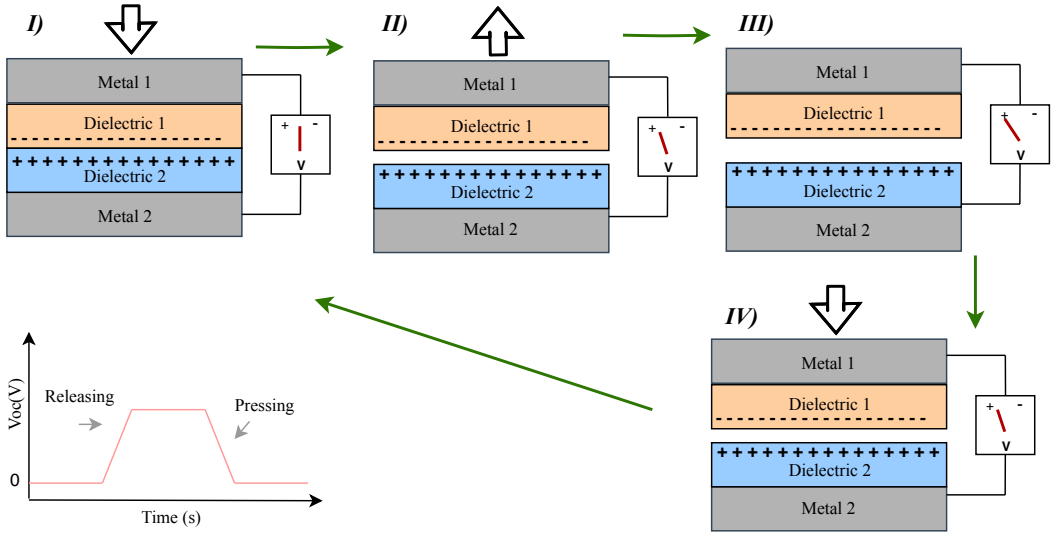

Figure 2.4: Operating principle of a TENG in a open-circuit condition (from [8]).

is reached (Fig. 2.4(III)). After the change on force direction, the opposite behavior will occur with the decreasing of distance (Fig. 2.4(III-IV)), until reaching the initial position.

In a short-circuit condition, the potential difference between electrodes will drive electrons from one electrode to another, resulting in an instantaneous positive or negative current, depending on the direction of movement (releasing or pressing – Fig. 2.5).

The *V-Q-x* relationship of the contact-mode can be derived base on electrodynamics [8], which is the most important equation to represent the behavior of a TENG. Under the assumption that the charge on the electrodes is uniformly distribute and the size area (S) is several orders larger than the separation distance ($d_1 + d2 + x$), the electric field inside the dielectrics and the air gap can be approximated as only a component in the perpendicular direction of the surface. Based on the equation of the electric field of parallel plates ($E = \frac{Q}{S\varepsilon}$) given by Gauss theorem, the electric field strength at each region is given by [8]:

Dieletric 1:

$$E_1 = \frac{-Q}{S\varepsilon_0\varepsilon_{r1}} \tag{2.4}$$

Air gap:

$$E_{air} = \frac{-Q}{S\varepsilon_0} + \frac{\sigma}{\varepsilon_0} \tag{2.5}$$

Dielectric 2:

$$E_2 = \frac{-Q}{S\varepsilon_0\varepsilon_{r2}} \tag{2.6}$$

Where ε_{r1} and ε_{r2} are the relative dielectric constant of dielectric 1 and dielectric 2, Q is the charge transferred between electrodes, σ is the charge density in the inner layer of dielectrics and d_1, d_2, $x(t)$ are the distances of each region (see Fig. 2.3(a)). So, the voltage between the two

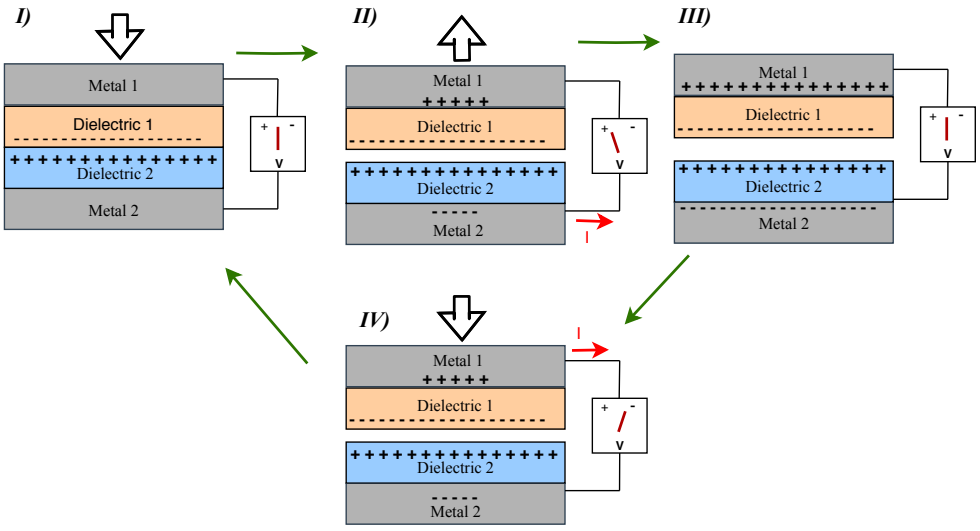

Figure 2.5: Operating principle of a TENG in a short-circuit condition (from [8]).

electrodes can be given by [8]:

$$V = E_1 d1 + E_2 d2 + E_{air} x \tag{2.7}$$

Combining 2.4, 2.5, 2.6 and 2.7 the *V*-*Q*-*x* relationship is found [8]:

$$V = \frac{-Q}{S\varepsilon_0}\left(\frac{d1}{\varepsilon_{r1}} + \frac{d2}{\varepsilon_{r2}} + x(t)\right) + \frac{\sigma x(t)}{\varepsilon_0} \tag{2.8}$$

Based on 2.1, the intrinsic output characteristics (V_{OC}, Q_{SC} and C) of this TENG mode, can be shown as:

$$V_{oc} = \frac{\sigma x(t)}{\varepsilon_0} \tag{2.9}$$

$$\frac{1}{C} = \frac{1}{S\varepsilon_0}\left(\frac{d1}{\varepsilon_{r1}} + \frac{d2}{\varepsilon_{r2}} + x(t)\right) \tag{2.10}$$

$$Q_{SC} = \frac{1}{S\varepsilon_0}\left(\frac{d1}{\varepsilon_{r1}} + \frac{d2}{\varepsilon_{r2}} + x(t)\right)\frac{\sigma x(t)}{\varepsilon_0} \tag{2.11}$$

2.4.2 Lateral Sliding Mode

This mode is the second mode and is based on in-plane charge separation mechanism. This mode also has two types: dielectric-to-dielectric (Fig. 2.6(a)) and conductor-to-dielectric (Fig. 2.6(b)).

In this mode with a dielectric-to-dielectric configuration, the top dielectric moves longitudinally in relation to the other dielectric, however the mechanism of creation the tribo-charges is the same as the previous mode. To obtain the model for this TENG mode it is considered that the width (w) of the whole structure is much larger than the thickness, and so, a 2D model can be used to simplify the calculation [17]. As shown in Fig. 2.6(a) the length of dielectrics is l in

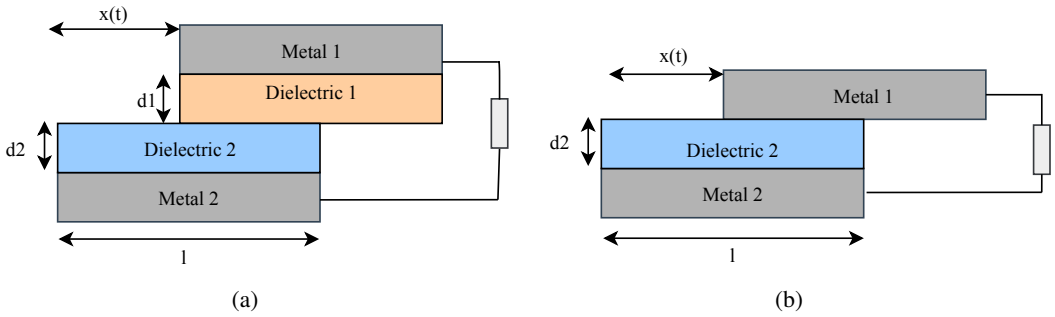

Figure 2.6: Lateral Sliding mode: (a) dielectric-to-dielectric and (b) conductor-to-dielectric.

the longitudinal direction, d_1, d_2 are the thickness of each dielectric and x is the lateral separation distance. After an initial contact between the two materials, when the dielectrics are displaced from one another (Fig. 2.7), the lower surface of dielectric 1 and the upper surface of dielectric 2 will have density charges with different signs, σ and $-\sigma$, respectively, due to the triboelectric effect. As in the previous mode, it is reasonable to assume that the tribo-charges are uniformly distributed at the two surfaces with negligible decay [17].

Figure 2.7 shows the principal mechanism of the lateral sliding mode. In an open-circuit conditions, the total charge at each metal electrode is zero and if an external path between the electrodes exists, the total charge amount on metal 1 and metal 2 will be -Q and Q, respectively. With the lateral movement of dielectric 1, a lateral polarization occurs by a mechanical force and creates a potential voltage across the electrodes. Consequently, a current will flow between metal 1 and metal 2, in order to cancel the potential induced by the tribo-charges, depending on the direction of movement (Fig. 2.7(II-IV)).

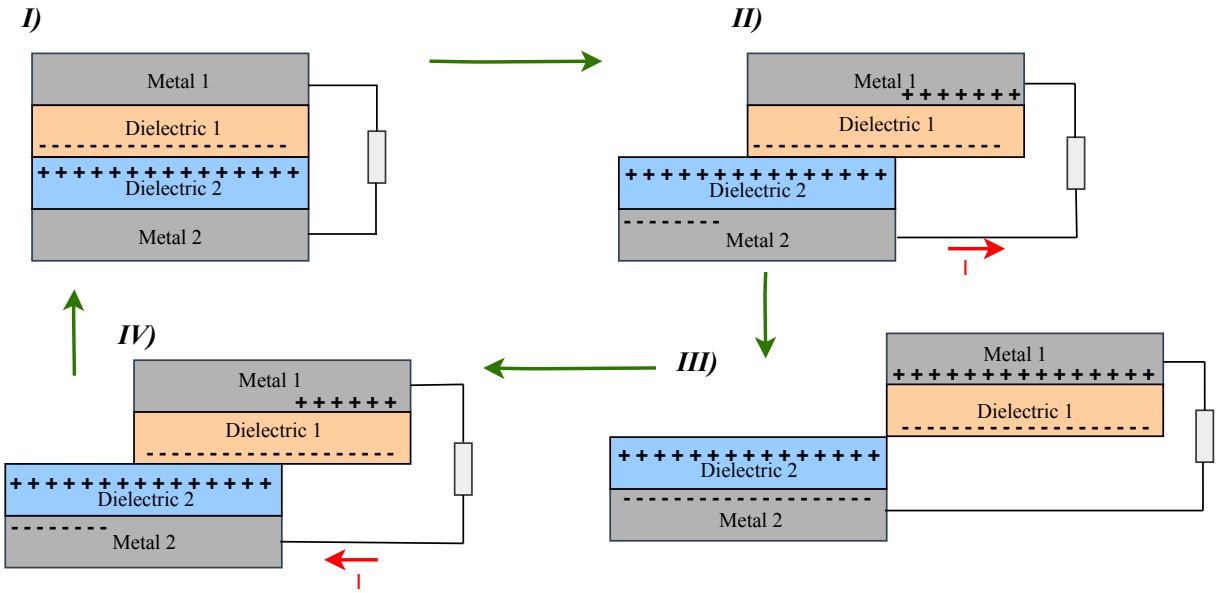

Figure 2.7: Working mechanism of the lateral sliding mode.

Using the assumption that l is always much larger that the thickness of the dielectrics, the theoretical analysis of this mode can be performed, obtaining the *V-Q-x* relationship.

Considering again the parallel-plate capacitor model, the contact area (S) in now changed taking into account the relative movement of the dielectrics, the C equation of this mode is given by [17]:

$$C = (\frac{\varepsilon_1}{d_1} + \frac{\varepsilon_2}{d_2})\varepsilon_0 w(l-x) \tag{2.12}$$

The V_{OC} equation can be estimated considering that the dielectrics width is much larger than the thickness. Consequently, the charge distribution can be approximated as uniform, and under open-circuit condition, the ideal charge distribution (ρ) can be represented by [17]:

$$\begin{cases} \rho = \sigma, & \text{For the non-overlapped region of the bottom electrode.} \\ \rho = -\sigma, & \text{For the non-overlapped region of the top electrode.} \\ \rho = -\frac{\sigma x}{l-x}, & \text{For the overlapped region of the bottom electrode.} \\ \rho = \frac{\sigma x}{l-x}, & \text{For the overlapped region of the top electrode.} \end{cases}$$

Based on the equation of the electric field of parallel plates given by Gauss theorem, the electric field strength at each region is given by:

$$\begin{cases} E_1 = \frac{\sigma x}{\varepsilon_0 \varepsilon_1 (l-x)}, & \text{For Dielectric 1.} \\ E_2 = \frac{\sigma x}{\varepsilon_0 \varepsilon_2 (l-x)}, & \text{For Dielectric 2.} \end{cases}$$

So, V_{OC} is given by:

$$V_{OC} = \frac{\sigma x d_1}{\varepsilon_0 \varepsilon_1 (l-x)} + \frac{\sigma x d_2}{\varepsilon_0 \varepsilon_2 (l-x)} \tag{2.13}$$

Replacing the V_{OC} and C in equation 2.1, the *V-Q-x* relationship can be obtained.

2.4.3 Single-Electrode Mode

In the modes presented above, the electrodes need to be connected to each other, which can limit their applicability [18]. This new mode overcomes this drawback, now, only one electrode is used, which is attached to (or serves as) the tribolectric layer (Fig. 2.8(a)) called primary electrode. The

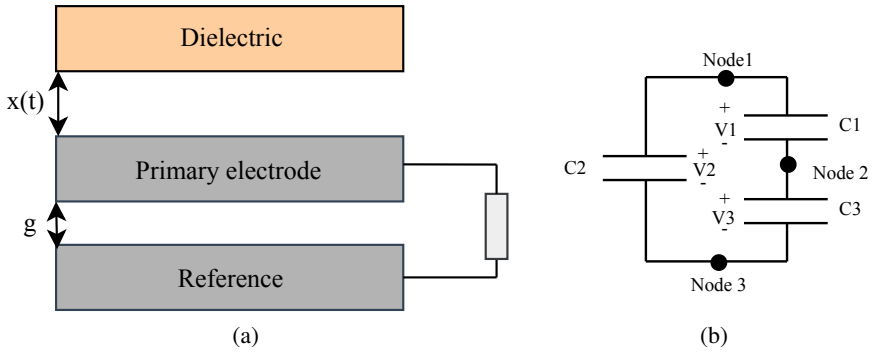

Figure 2.8: Single-electrode mode: (a) diagram and (b) the equivalent circuit model.

other electrode is used as an electric potential reference, called reference electrode, and can be connected directly to ground, for example.

The dielectric layer and electrode (primary electrode) are stacked face to face to form the triboelectric pair, with the same length (l) and width (w). Under an external mechanical force, the dielectric moves relative to the two fixed electrodes, changing the distance (x) between the two triboelectric pairs. Such as, the previous mode, with the contact of the two pairs, the surface of dielectric and the electrode (also works as dielectric) becomes loaded with opposite charges. Assuming that the charges are uniformly distributed on the surface of materials, the amount of charges induced in the primary electrode is ($\sigma \cdot l \cdot x$). If a external path between the primary and reference electrode exist, Q charges will be transferred and the total amount of charges will be ($\sigma \cdot w \cdot l - Q$) and Q in each electrode, respectively (Fig. 2.8).

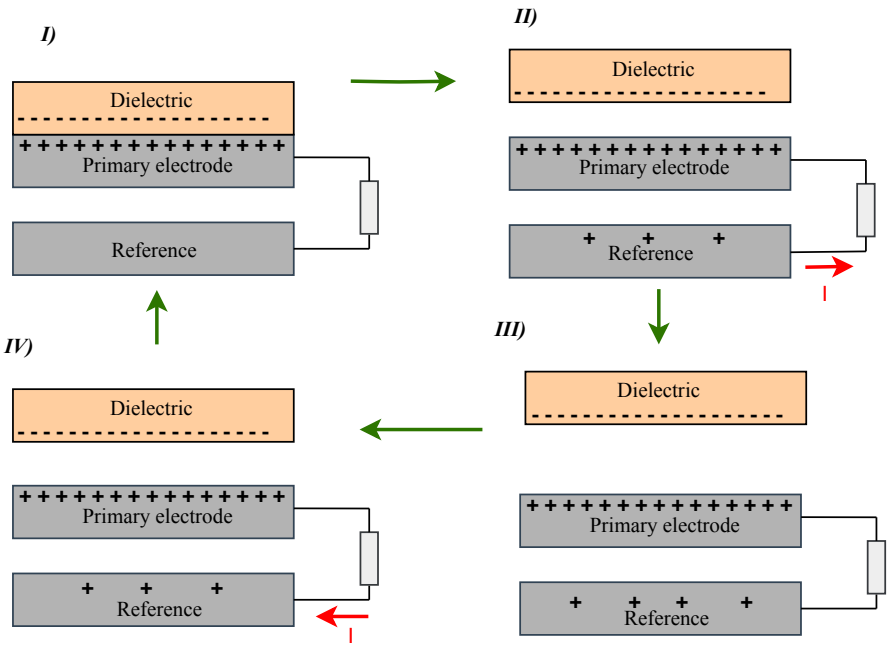

Figure 2.9: Working mechanism of the single-electrode mode.

In that case, in order to estimate V_{OC} and C, a theoretical equivalent circuit model, based on the

nodes of the electrostatic system can be used. One node corresponds to a surface/volume with a specific electric potential [18]. In an open-circuit condition the total charges on dielectric bottom surface (Node 1), primary electrode (Node 2) and reference electrode (Node 3) are $(-\sigma \cdot w \cdot l)$, $(\sigma \cdot w \cdot l)$ and 0, respectively. So each of these surfaces can be defined as a node and since every two nodes are connected by electric field lines, an equivalent capacitance is formed between each of them. Figure 2.8(b) represents the equivalent circuit containing three "virtual" capacitors. These capacitors only represent the capacitance effects from the direct electric line connection between every two nodes, therefore, the electrostatic shield of the third capacitor is not considered. Based on that, the capacitance between Nodes 2 and 3, that represent the C value, is given by [8]:

$$C = C_3 + \frac{C_1 C_2}{C_1 + C_2} \tag{2.14}$$

From basic characteristics of capacitance and charge conservation, the following equations can be derived:

$$V_2 = V_1 + V_3 \tag{2.15}$$

$$C_2 V_2 + C_1 V_1 = -\sigma w l \tag{2.16}$$

$$-C_1 V_1 + C_3 V_3 = \sigma w l \tag{2.17}$$

Combining the previous equations, the V_3 at open-circuit condition (V_{OC}) is:

$$V_3 = V_{OC} = \frac{\sigma w l C_2}{C_1 C_2 + C_2 C_3 + C_3 C_1} \tag{2.18}$$

And under short-circuit condition:

$$Q_{SC} = V_{OC} C = \sigma w l \frac{C_2}{C_1 + C_2} \tag{2.19}$$

Based on equation 2.14, is easy to conclude that C is nearly constant, imposed by the C_3 value, which is fixed because the primary electrode and the reference electrode is fixed. In this configuration the Q_{SC} is half the value for the other modes. The explanation for that it is that, when dielectric 1 is far from the electrodes, the tribo-charges generated are equally distributed between the two electrodes (shield effect of their primary electrode) to maintain the two electrodes at the same potential, that leads to a charge transfer efficiency (η_{CT} - ratio between Q_{SC} and the amount of tribo-charges) of only 50%, while the others modes can reach nearly 100% [18].

2.4.4 Freestanding Triboelectric -Layer Mode

As discussed in the previous mode, the efficiency of the single-electrode mode is only half of the other modes. To overcome this drawback, another mode was presented, called freestanding

triboelectric layer mode. In this mode, such as in the previous one, the dielectric layer moves freely and electrodes are fixed. However, now the tribo-charges surface alternatively approach the two electrodes [8].

This mode has two different architectures, both based in the same working principle, the contact-mode and sliding-mode (Fig. 2.10 and Fig. 2.11, respectively). These architectures have different output characteristics, and so, will be discussed separately.

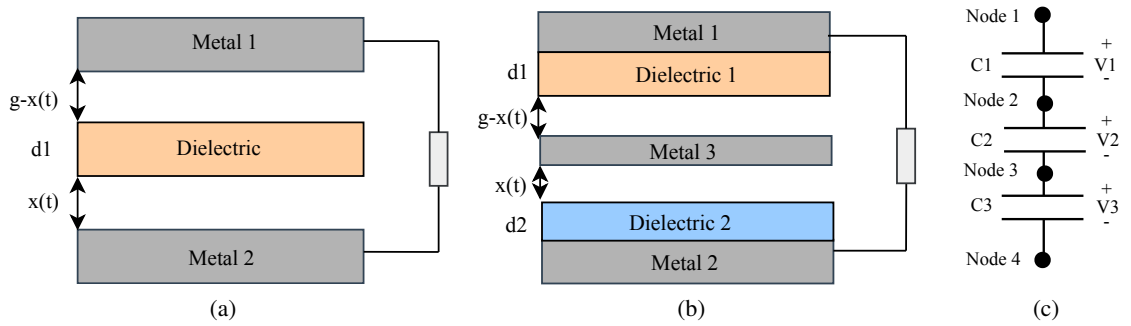

Figure 2.10: Contact freestanding mode: (a) Dielectric freestanding layer and (b) metal freestanding layer. (c) Equivalent circuit model.

Contact-Mode Freestandig TENG

The two typical structures of a contact-mode freestanding TENG are shown in Figure 2.10 [19], with the same working mechanism. In the first configuration, a dielectric plate and two metal plates are stacked face to face, forming two pairs. Due to an external force, the dielectric plates is forced to contact with the top and bottom metal plate, and will create static triboelectric charges on surfaces of dielectric and electrodes (Metal 1 and Metal 2). For simplicity, and based on charge conservation is assumed that the triboelectric charge density of both dielectric surfaces is $-\sigma$ and that the two metal plates will have the same amount of positive charges in total.

To do the electrostatic analysis, the concept of nodes can be used again. Since normally the size of the metal electrode is much larger than the air gap, the edge effect can be ignored. As a result, the electric potential on metal 1, metal 2, top and bottom surface of dielectric are all constant [8], and so, 4 nodes can be defined in this system. Since the electrical line connection between every two nodes forms an equivalent capacitance, the model of Figure 2.10(c) can be deduced. The total capacitance between the node 1 and 4 of the first configuration (Fig. 2.10(a)), is the serial connection of the three capacitors. The total capacitance is given by [19]:

$$C = \frac{1}{\frac{1}{C_1} + \frac{1}{C_2} + \frac{1}{C_3}} = \frac{\varepsilon_0 S}{g} + \frac{\varepsilon_0 \varepsilon_1 S}{d1} \tag{2.20}$$

,where d_1 is the thickness of the dielectric layer and g is the total gap between electrodes.

Under short-circuit condition, the charges on each node need to be deducted to solve this electrostatic system. For nodes 2 and 3, the amount of charge in each node is $(-\sigma \cdot S)$. Due the

charge conservation, the total charge on Node 1 and Node 4 are ($2\sigma \cdot S$), where the charge in each node is still unknown. However, defining that the charge in node 1 (metal 1) is Q_1, the total charge in node 4 (metal 2) is ($Q_2 = 2\sigma \cdot S - Q_1$). From the basic electrodynamics theory and charge conservation, the following equation set can be obtained [19]:

$$V_1 = \frac{Q_1}{C_1} \tag{2.21}$$

$$V_2 = -\frac{\sigma S - Q_1}{C_2} \tag{2.22}$$

$$V_3 = -\frac{2\sigma S - Q_1}{C_3} \tag{2.23}$$

$$V_1 + V_2 + V_3 = 0 \ (Short - Circuit\ condition) \tag{2.24}$$

From the above equation set, the total charges on each metal is given by:

$$Q_1 = \sigma S \frac{\frac{1}{C_2} + \frac{2}{C_3}}{\frac{1}{C_1} + \frac{1}{C_2} + \frac{1}{C_3}} \tag{2.25}$$

$$Q_2 = \sigma S \frac{\frac{2}{C_1} + \frac{1}{C_2}}{\frac{1}{C_1} + \frac{1}{C_2} + \frac{1}{C_3}} \tag{2.26}$$

In practical applications, the value of C_2 ($C_2 = \frac{\varepsilon_0 \varepsilon_1 A}{d1}$) can be seen as infinitely large, because d_1 is always negligible compared to the air gap. So the above equations can be simplified in [19]:

$$Q_1 \approx \sigma \frac{\frac{2}{C_3}}{\frac{1}{C_1} + \frac{1}{C_3}} = \frac{2\sigma S}{1 + \frac{C_3}{C1}} \tag{2.27}$$

$$Q_2 \approx \frac{2\sigma S}{1 + \frac{C_1}{C_3}} \tag{2.28}$$

With this equations the basic working mechanism can be observed. When $x = 0$, C_3 is infinity. As a result, Q_1 is close to 0 and Q_2 is approximately ($2\sigma \cdot S$). While when the distance ($x = g$), C_1 is infinity and all the positive charges on the electrodes are attracted to metal 1.

Thus, when the dielectric moves inside the air gap, charges will alternatively flow between the two electrodes due to the change of (C_1/C_3) that will drive electrons to flow between the two electrode.

The short circuit transferred charges (Q_{SC}) is given by [19]:

$$Q_{SC} = \frac{2\sigma S x}{\frac{d_1}{\varepsilon_1} + g} \tag{2.29}$$

Based on equation 2.1 the V_{OC} can be obtained as [19]:

$$V_{OC} = \frac{Q_{SC}}{C} = \frac{2\sigma x}{\varepsilon_0} \tag{2.30}$$

So, the $V - Q - x$ relationship can be show as:

$$V = -\frac{1}{C}Q + V_{OC} = -\frac{\frac{d1}{\varepsilon_1} + g}{\varepsilon_0 S} + \frac{2\sigma x}{\varepsilon_0} \tag{2.31}$$

Sliding-Mode Freestandig TENG

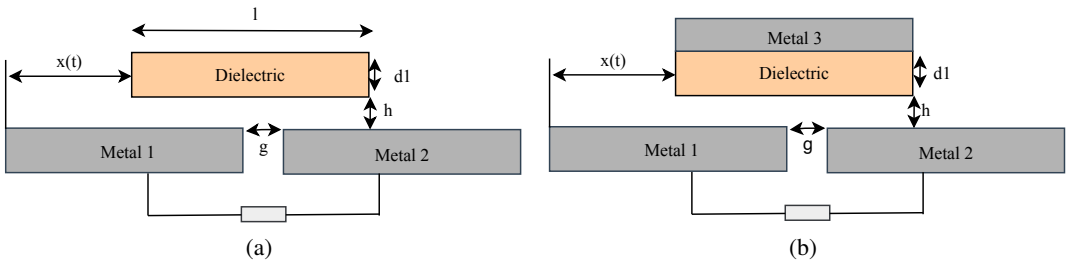

Figure 2.11: Sliding freestanding mode: (a) dielectric freestanding layer and (c) metal freestanding layer.

The other architecture of a freestanding TENG also has two different structures as shown in Figure 2.11. The metal 1 and metal 2 are placed in the same plane with the gap g, to form two electrodes [19]. In Figure 2.11(a), the freestanding material is only the dielectric and in structure of Fig. 2.11(b) a thin layer of metal is deposited at the backside of the dielectric. These structures are very similar with the contact-mode freestanding architecture, but the freestanding material, in this case, strongly influences the output characteristics. Only the first structure (Fig. 2.11(a)) will be analyzed.

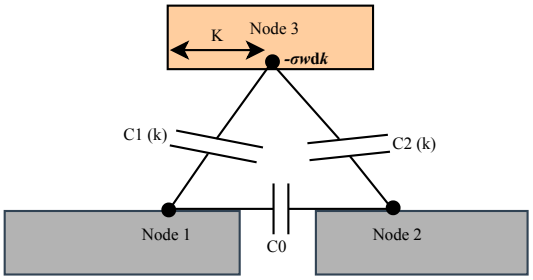

Figure 2.12: Equivalent circuit model of the dielectric freestanding layer mode

The node concept can still be used to analyze this structure (Fig. 2.12(a)). However, now the electrical potential of the bottom surface is not constant and could not be seen as a single node [8]. To solve this problem the electric potential superposition principle of small regions have to be used. Assuming that only a small region of $d \cdot k$ (k - distance to the left edge of the bottom dielectric

surface) in the bottom dielectric surface contains the tribo-charges with density of $-\sigma$, the total charges on metal 1 and 2 are ($\sigma \cdot w \cdot dk$). Under short-circuit condition, the electrical potential in nodes 1 and 2 will be the same. Thus, from the charge conversation and electrodynamics the total charge on metal 1 and metal 2 (dQ_1 and dQ_2), the following equations are satisfied [19]:

$$\frac{dQ_1}{C_1(k)} = \frac{dQ_2}{C_2(k)} \tag{2.32}$$

$$dQ_1 + dQ_2 = \sigma w dk \tag{2.33}$$

From these equations, dQ_1 and dQ_2 can be defined as:

$$dQ_1 = \frac{\sigma w dk}{1 + \frac{C_2(k)}{c1(k)}} \tag{2.34}$$

and

$$dQ_2 = \frac{\sigma w dk}{1 + \frac{C_1(k)}{c2(k)}} \tag{2.35}$$

The total charges on metal 1 and metal 2 is the integration of each small tribo-charged region. So the total transferred charges ($Q1_{SC}$) in a movement of the dielectric ($Q_1(x = g + l) - Q_1(x = 0)$) is given by [19]:

$$Q_{SC} = \int_0^l \frac{\sigma w dk}{1 + \frac{C_2(k)}{C_1(k)}_{x=g+l}} - \int_0^l \frac{\sigma w dk}{1 + \frac{C_2(k)}{C_1(k)}_{x=0}} \tag{2.36}$$

When $x = 0$, Q_1 will be approximately σwl and when $x = g + l$ it will be 0. Thus, Q_{SC} can reach σwl and the charge efficiency (η_{CT}) can get as far as 100 %.

So as presented, different TENG configurations can be used to convert mechanical energy into electricity. These modes can be used to harvest all kinds of mechanical energies that are available but wasted in our daily lives. Now, this technology can provide micro-scale power for small electronics or could be the basis of harvesting mega-scale energy, and so, it has the potential of making a huge contribution to the sustainable energy for the world.

Chapter 3

Triboelectric nanogenerator design for random water wave movements

In order to create a solution that can satisfy the power requirements of electrical systems for maritime applications, a TENG implementation will be realized. As shown in chapter 1, several TENGs implementations have been presented for water wave energy harvesting in the last years, showing how promising this technology can be for harvesting energy in the ocean conditions [9–12, 20, 21]. To harvest this energy, which is mostly present in the movement of random waves with low-frequency [4], the implementation that will be realized should be able to work in such conditions.

The motivation and the evolution of our triboelectric nanogenerator design will be explained in this chapter. Two different TENG implementation will be presented here, however, only one will be adopted for the final system. Moreover, the production methods used to fabricate the TENG will also be detailed.

3.1 First TENG implementation

Inspired on some solutions already published [9–12, 20, 21], a first implementation has been defined. Using a spherical metal structure has been attempted to implement the triboelectric materials on the interior walls of this structure, in which smaller metal spheres were placed inside it (Fig.3.1(a)), to promote the contact of materials based on vertical contact-separation TENG mode, see Figure 2.4.

To built this TENG, two dissimilar dielectric (Polytetrafluoroethene-PTFE and Nylon 6.6) films were faced with each other with an electrode attached to each tribo material, as depicted in Fig.3.1(b). A copper film was attached to the bottom surface of PTFE film and a silver film was deposited on the top surface of Nylon. These two triboelectric materials have been chosen in order to enhance the electronegativity difference of materials, based in the triboelectric series. The electrodes material was chosen to ease their application in triboelectric material. Under an external random movement, the metal spheres will roll inside the spherical structure and on top of

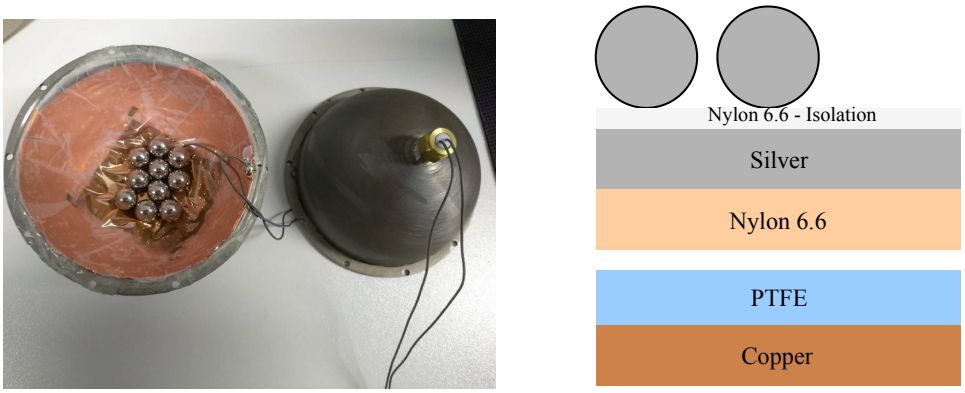

(a) (b)

Figure 3.1: First implementation tested: (a) photography of TENG and (b) schematic of it layers.

TENG, pressing and releasing the triboelectric materials, creating a potential voltage between the electrodes (see Fig. 2.4 with the working mechanism).

However, due to the rigidity of the materials, it was not possible to cover the whole interior surface of the metal sphere, and so, this implementation was discarded. Therefore, we decided to evolve to a flat implementation, where the same materials were deposited in the same order. Figure 3.2(a) shows the new implementation, in which the TENG was built in a $9\,\text{cm} \times 9\,\text{cm}$ metal plate, that was also placed inside the metal spherical structure (Fig.3.2(b)), with the same operating principle as the previous attempt.

Although with this new implementation we overcome the deposition material problems, the first experimental results were not very satisfactory. Different ball sizes, different numbers of balls and different number of TENG layers were tested. Measuring the voltage in open-circuit was concluded that with heavier balls and increasing the number of balls the performance slightly improve. However, increasing the number of tribo-pairs, as depicted in Figure 3.3(b), with two tribo-pairs and connected them in series, the results did not improve as expected. The reason for that could be again the rigidity of the materials, that mainly affects the movement of the bottom layers. With a controlled movement (one direction movement with the structure showed in Fig. 3.3(c)) was reached a maximum open-circuit voltage of 5V (Fig. 3.3(a)) and a power density of $7.8\,\mu\text{W}/\text{m}^2$, with one layer and 6 metal spheres inside.

Therefore, with the problems with the rigidity of the materials, the low performance results and the difficulty in experimentally optimize this implementation, it was decided to evolve to another implementation, based on another fundamental mode.

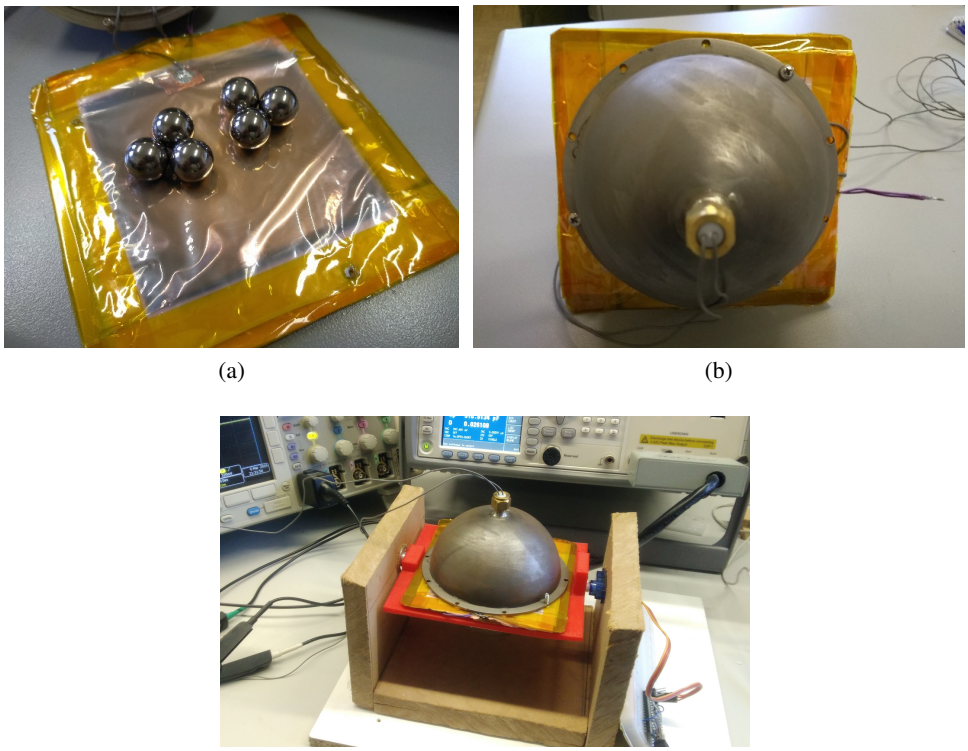

(a) (b)

(c)

Figure 3.2: Flat implementation TENG: (a) TENG implementation with six metal spheres on top and the (b) spherical support structure, (c) structure (first attempt) to recreate a oscillating movement.

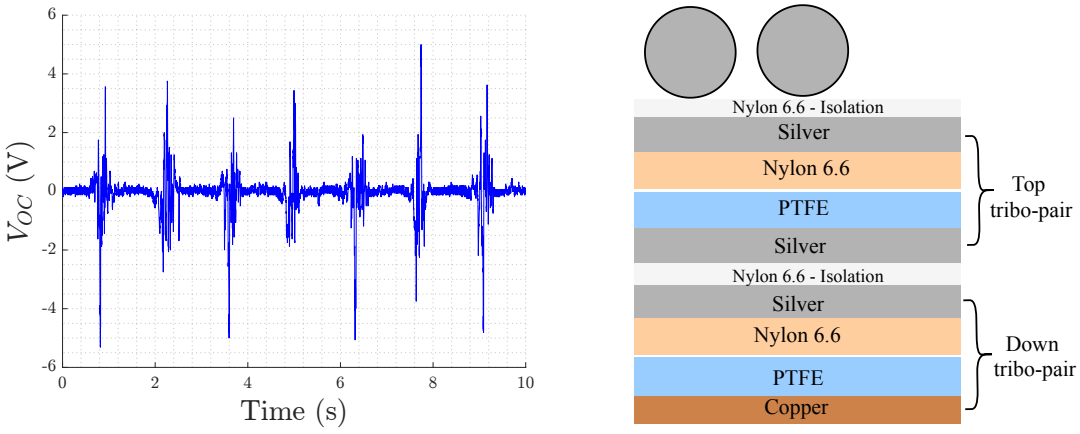

(a) (b)

Figure 3.3: (a) V_{OC} plot of the flat TENG implementaion and (b) schematic with two tribo-pair layers (top tribo-pair and bottom tribo-pair).

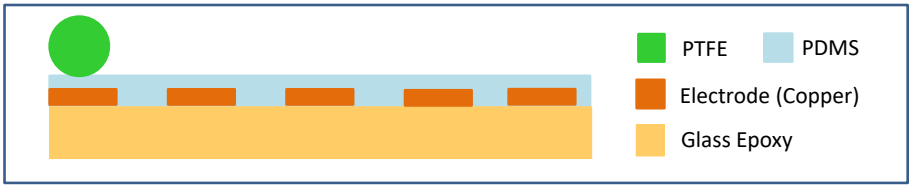

(a)

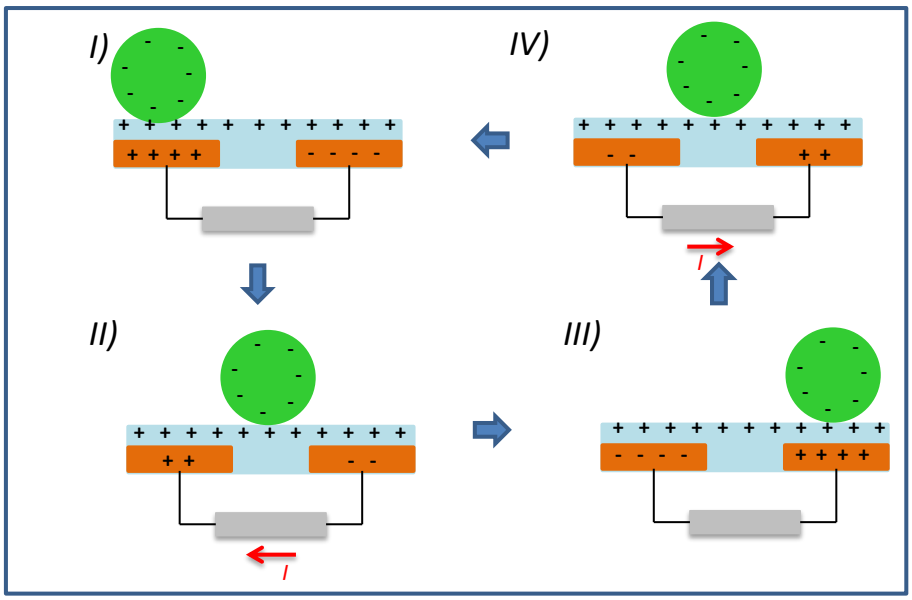

(b)

Figure 3.4: Second TENG implementation: (a) schematic diagram of the proposed implementation and (b) its working mechanism.

3.2 Second TENG implementation and working mechanism

A totally new approach was therefore followed, based on a different triboelectric nanogenerator mode. This new implementation has to be easy to fabricate, overcoming the problems with the materials and also has to work in environments with random movements.

Following the same ideas as in the previous implementation, where metal spheres capture the random movements of the environment and convert them into an electrical signal, it was decided a new approach also based in the free movement of spheres. In the previous design, the metal spheres were used to promote the contact between the two triboelectric materials, pressing and releasing the triboelectric materials. In this approach we also used spheres, but with the difference that now they act as a triboelectric material, carrying charges. This approach is based on the sliding freestanding mode (showed in Fig. 2.11), where one of the triboelectric layers moves freely (the spheres) and the other is fixed. Similar solutions [9, 11] presented for ocean wave energy, also use this same principle.

Figure 3.4(a) shows the diagram of the intended implementation, in which a printed circuit board (PCB) was printed two copper patterns that act as electrodes and on top was coated a poly-dimethylsiloxane (PDMS) film as triboelectric material. After that, triboelectric spheres were

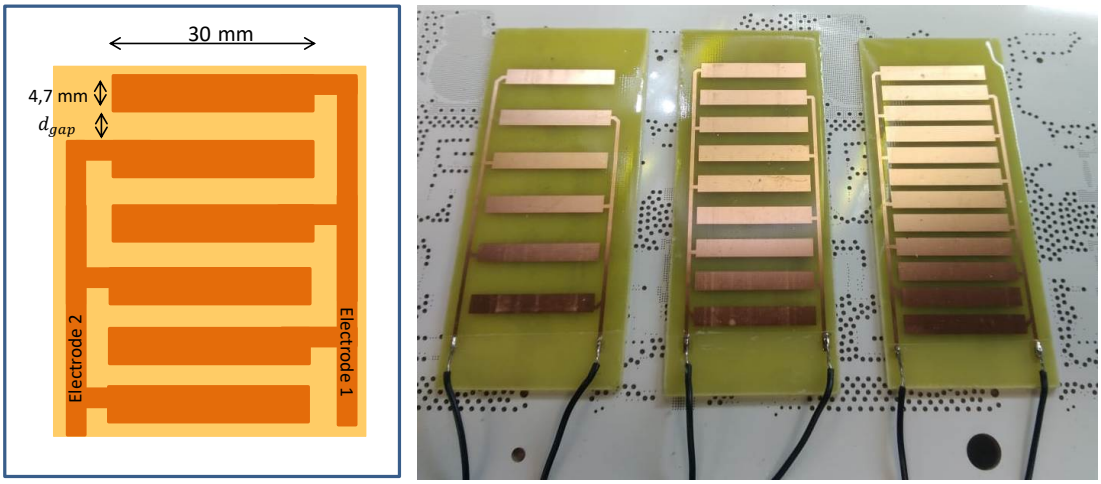

(a) (b)

Figure 3.5: (a) Diagram of the copper pattern and the (b) photography of the printed electrodes on PCB with different values of d_{gap} (2.5mm, 5mm and 9.5mm, respectively).

placed on top of the PCB, to move freely and touching alternately the electrodes.

The working principle of this new implementation is described in Figure 3.4(b), in which four major steps are involved. Under the excitation of an external force, the spheres roll back and forth between electrodes. After multiple cycles of contact between the spheres and the triboelectric material on top of the PCB charges are induced in each material (Fig. 3.4(b)-I), based on the triboelectric effect. When the spheres roll to the right, the charges previous accumulated in spheres will induce charges on the opposite electrode, and a current flow will occur via an external load to keep the charges balanced (Fig. 3.4(b)-II). When the spheres are overlapped with the electrode the flow of charges stops and the first half cycle is accomplished. In the same way, when the spheres rollback, the charges will flow in the opposite direction (Fig. 3.4(b)-III-IV).

The copper pattern printed in PCB with 8 cm $\times$ 3 cm is showed in Figure 3.5.(a), with copper strips with a width and height of 30mm and 4.7mm, respectively. These dimensions are imposed based on the sizes of the spheres that will be used. In order to try to optimize this implementation different values of d_{gap} (spacing between the copper strips) were tested, with values of: 2.5mm, 5mm and 9.5mm (Fig. 2.3). The optimization of this device will be systematically presented in the next chapter.

3.3 Materials selection and manufacturing process

As already discussed, the two triboelectric materials should be selected in order to ensure that they have opposite triboelectric polarities. Based on the materials available and considering the suitability of depositing the material in the PCB surface, PDMS was chosen to be applied in the PCB. For the materials of the spheres, we had available several spheres of different materials but we predicted, based on the triboelectric series, that the best material available to use was Nylon 6.6.

(a)

Figure 3.6: Photography of different size PTFE spheres.

However, this was not observed experimentally, as will be showed in the next chapter. The final triboelectric materials used on this device were the PDMS on top of PCB and spheres of PTFE. Figure 3.6 shows the PTFE spheres used, where different sizes were tested, as will be presented in chapter 5.

To apply the PDMS on the top of the PCB was used the spin-coating technique, that allow to deposit uniform thin films onto flat substrates. By means of a rotation force, the material is spread and uniformly coats its surface. Knowing the viscosity of the material it is possible to control the thickness of the PDMS film with precision by controlling the rotation speed of the spinner. The higher the rotation speed uses, the thinner the thickness of the PDMS film.

All this process is shown diagrammatically in Figure 3.7. A PDMS solution was deposited on top of the PCB and with a rotation speed of 500 rpm in 30 seconds was accomplish a thickness of 220 µm. After that, the film was cured by placing the film and the PCB at 85 °C for 2 hours.

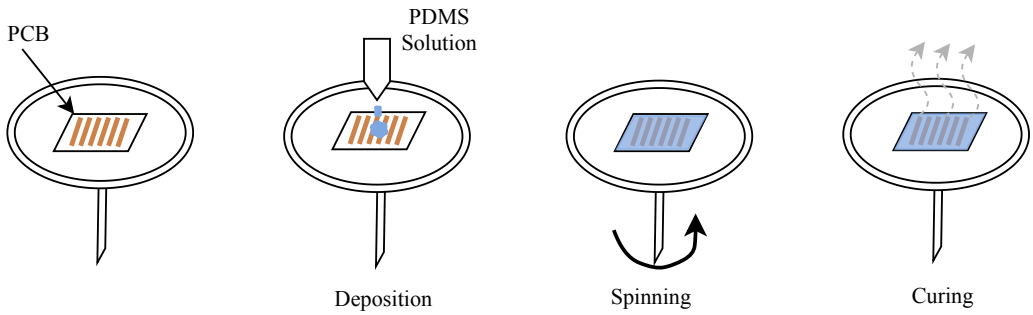

(a)

Figure 3.7: Spin-coating process.

3.4 Support structures

To support the PCB and the spheres, a structure was created in Solidworks software and printed in a 3D printer with polylactide (PLA) material. The box structure in Figure 3.8(a) with 4 cm × 10 cm × 5 cm of dimensions, was created to be fixed to the motion creator structure (presented in next chapter) and to support one of the PCB and the several triboelectric spheres. Also, another structure was created to support several units at the same time (Fig.3.8(b)). This structure was developed to fix three PCBs. The reason for that will also be explained in the next chapter.

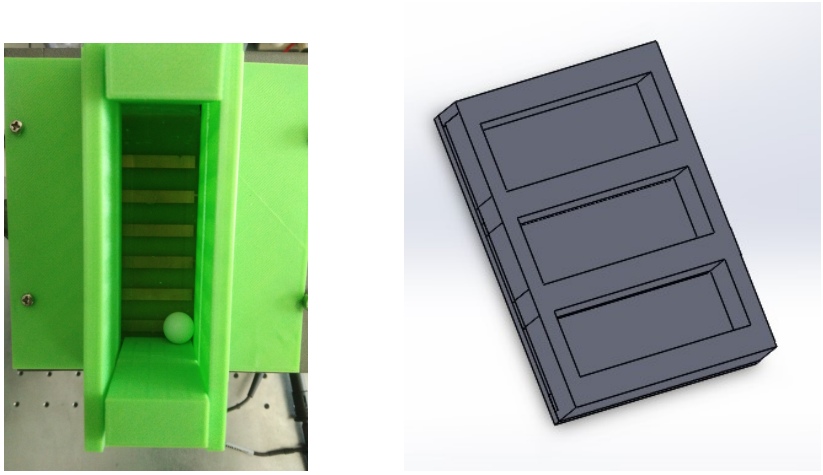

(a) (b)

Figure 3.8: (a) Photography of the support structure used for test of one unit and (b) a Solidworks image capture of the structure created to support three units.

Chapter 4

Measurement Setup

Systematic methods and devices developed to acquire the data to evaluate the performance of the proposed TENG will be presented.

4.1 Ocean motion simulation

In order to evaluate the performance of the proposed TENG and since the purpose of this device is to harvest energy from ocean environments, mainly characterized by an ondular motion, the experimental measurements should be realized under similar conditions. For that, a metal structure was built with an axis coupled to a servo motor, recreating an ondular movement in one direction. Figure 4.1(a) shows the U-shaped metal structure built, where an axis was coupled by two pulleys in each tip (Figure 4.1(c)). In one of the axis tips was coupled a servo motor by a metal gear, in order to transfer the rotation motion to the main axis.

The servo motor (MG995R) (Figure 4.1(d)) was chosen based on the torque provided and in the operating voltage, in which a torque of $8.5\,\mathrm{kgf \cdot cm}$ at $5\,\mathrm{V}$ is more than enough for our implementation. The servo motor was controlled by a PWM (Pulse Width Modulation) pulse generated by an Arduino nano. The microcontroller produces a digital square wave, where the frequency is constant ($50\,\mathrm{Hz}$), but the fraction of the time that the signal is on (the duty cycle) can be varied. Thus, varying the duty cyle of the square wave is possible to control the position of the axis. A C++ code was upload to the microcontroller to create an oscillatory motion of the axis of 45 degrees for each side, with a velocity of 60 degrees/sec, as depicted in Figure 4.2. This velocity was imposed to create a slow rotation movement of the axis, in order to simulate an ocean wave motion of $1.5\,\mathrm{Hz}$. Figure 4.1(b) shows the structure with the 3D printed box with one TENG unit attached to it, which was the implementation used for tests presented in chapter 5.

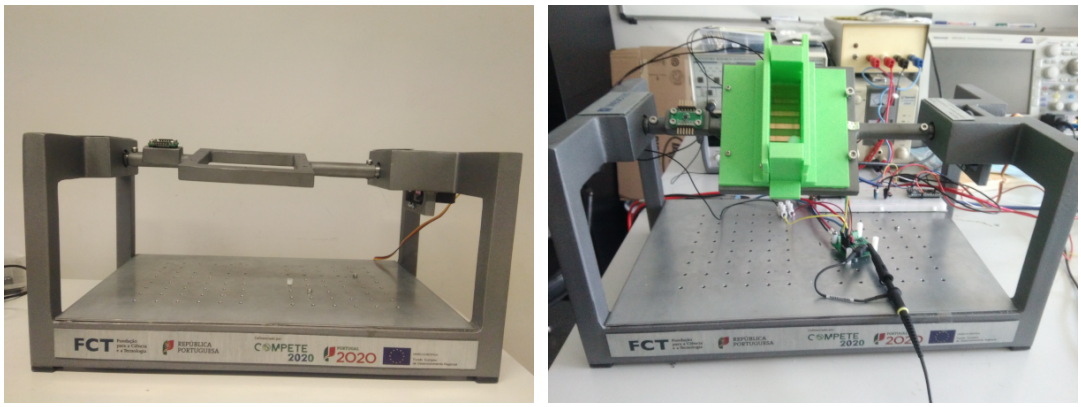

(a) (b)

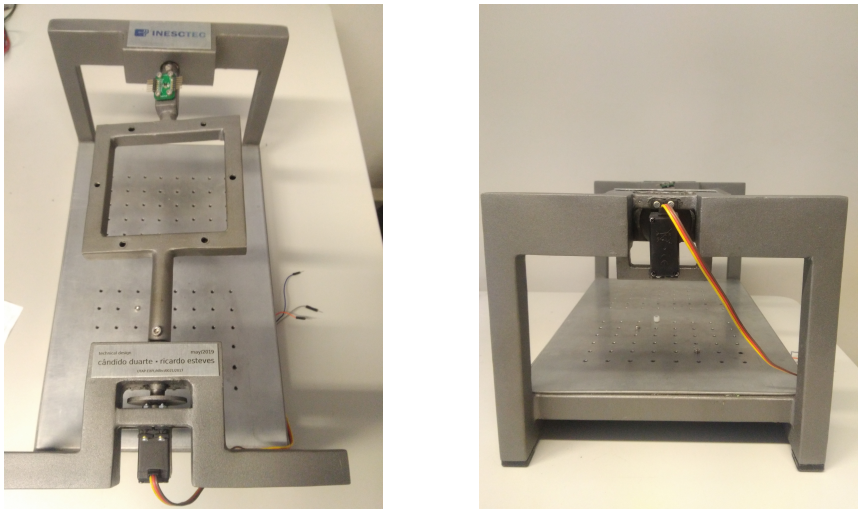

(c) (d)

Figure 4.1: (a-c) Metal structure built to mimic the ocean waves in different perspectives.

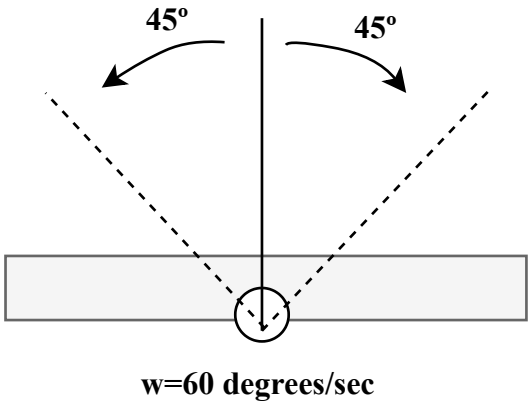

Figure 4.2: Diagram of the axis movement.

4.2 Voltage and current measurements

Two of the metrics used to evaluate the performance of the TENG were the open-circuit voltage (V_{oc}) and the short-circuit current (I_{SC}) [22]. To perform the acquisition of the open-circuit voltage was used an oscilloscope (Tektronix MDO3014) [23] with a high-impedance ampop in a buffer configuration to minimize probe loading effects. More details about this strategy will be given in the next subsection.

To measure the short-circuit current and since, the current generated by the TENG is very low, was measured the voltage drop on a precision resistance of 100Ω ($\pm$ 1%). However, due to the low voltage drop, a low noise preamplifier (Standford SR560) [24] had to be used to amplify that signal, that was connected to the oscilloscope to acquire the signal, and so, calculate the current. To obtain in oscilloscope the cleanest possible signal, the preamplifier was configured with a high-pass filter at + 6 dB/octave and a low-pass filter at + 6 dB/octave, and cutoff frequencies of 1 Hz and 300Hz, respectively, with a gain of 1000.

4.3 Load characterization

Another important measurement that will be presented, is the performance evaluation under different load resistances. Since normally the optimum load of a TENG is in the order of mega ohms [15] and with the objective to automate the load sweep measurements, a multiplier resistance opamp based circuit [25] was built to simulate high resistances. The circuit showed in Figure 4.3 is a voltage follower with an input resistance that depends on resistors $R1$, $R2$ and $R3$, which are resistors with standard values. Varying the value of resistor $R3$ the input impedance can be controller, under the following equation:

$$Z_{in} = R_2 + R_3\left(\frac{R_2 + R_1}{R_1}\right) \tag{4.1}$$

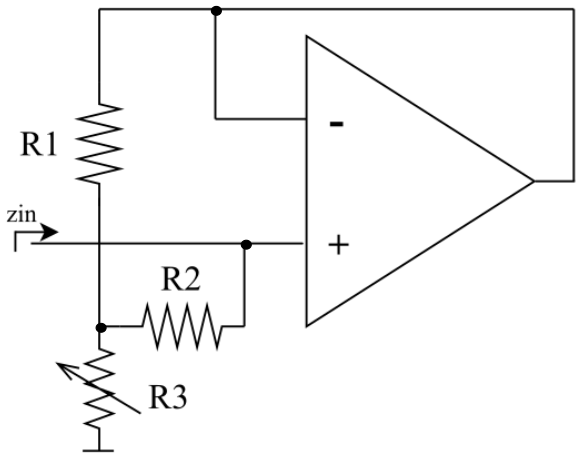

Figure 4.3: Multiplier resistance opamp based circuit.

Choosing the proper values for the resistor R_1 (510 Ω) and R_2 (1.4 MΩ) and using a digital potentiometer on place of R_3, the input impedance (Z_{in}) of this configuration can be controlled digitally. Varying R_3 from 250 Ω to 500 KΩ a Z_{in} range between 1.4 MΩ and 1.4 GΩ can be obtained.

For this implementation was chosen the OPA828 ampop of Texas Instruments because it presents a high input impedance (1 TΩ) and has a wide supply voltage range of ±18 V. High input impedance is required in order to not affect the multiplier resistance configuration, and a wide supply voltage to not constrain the voltage swing of TENG signal. To validate this behavior, this configuration was first simulated in TINA software, using the ampop model provided by the manufacturer. The result obtained by simulation is shown by the red line in the plot of Figure 4.4.

After that, it was decided to develop the PCB with this circuit. For the digital potentiometer was chosen the AD5235 of Analog Devices, a 1024-position digital potentiometer controlled by a serial peripheral interface (SPI).

In the same board, for lowers resistance values, two digital potentiometers was connected in series, given a total controlled resistance between 250 Ω and 1 MΩ. So, two resistances chains are presented in the board, one for low values and other for high resistance value, that can be selected by a jumper presented on the board, as depicted in Figure 4.5(a). The Eagle Cad schematic of the developed board can be found in Appendix A.

After the printed board assembled (Fig.4.5(c)), was performed the experimental validation of the circuit, measuring the input impedance with a high range multimeter (Keysight 34401A) [26]. The characterization results are presented by the blue dots in the plot of Figure 4.4, here the expected behavior is showed, in which controlling the digital potentiometer (R_3) it was able to control the input impedance. The slight difference for resistance above 600MΩ between the simulated and experimental results, it is due to the error of the multimeter to measure high resistances.

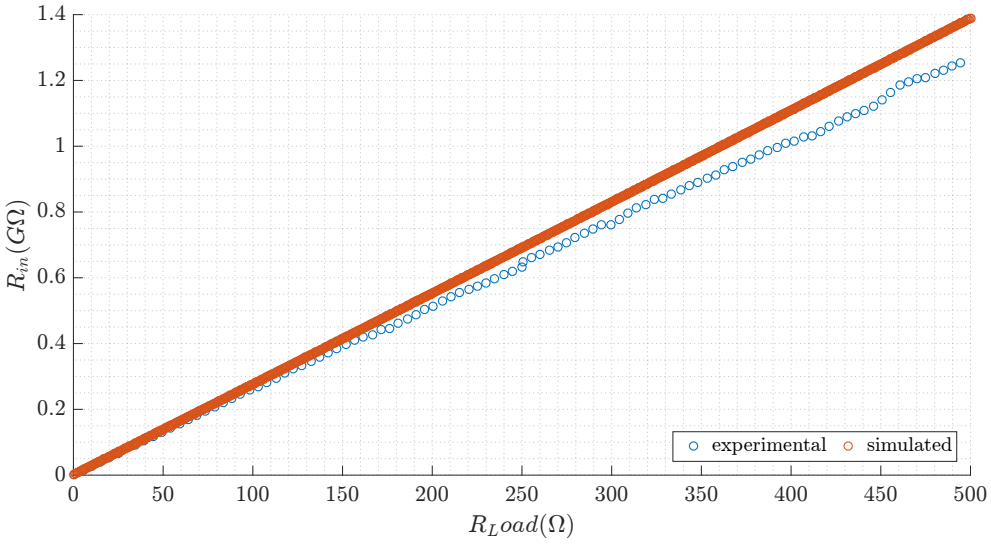

Figure 4.4: Simulated and experimental results of the impedance multiplier board.

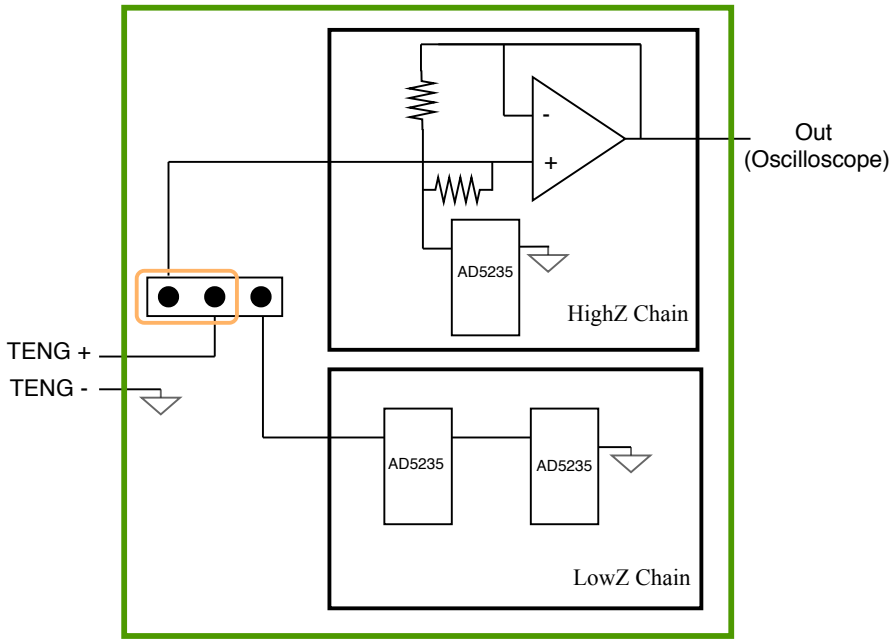

(a)

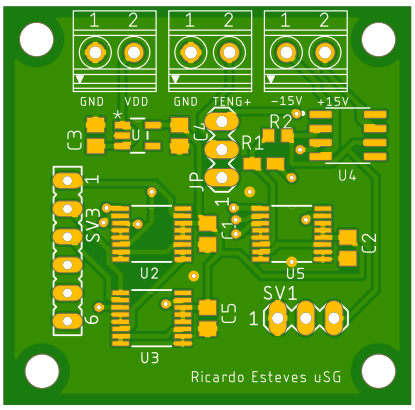

(b)

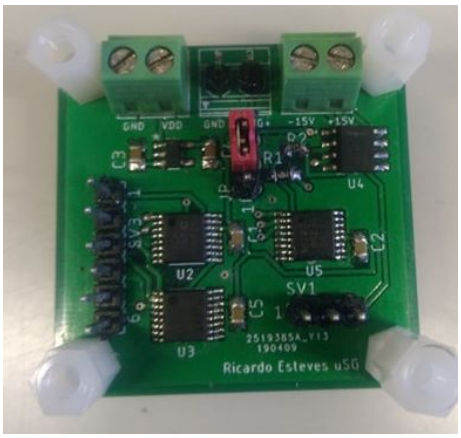

(c)

Figure 4.5: (a-c) Diagram of the board developed and (c) photography of the assembled board.

4.4 Automated measure process

To automate the data acquisition process, the setup configuration presented in Figure 4.6 was used. Two types of measurements were performed, the open-circuit voltage and the short-circuit current, as discussed above. The open circuit voltage was acquired using the oscilloscope with the impedance multiplier board in the maximum position of scale (1.4 GΩ), behaving as a buffer element. The short-current was measured with a precision resistance placed in a breadboard, and acquired the voltage drop with the oscilloscope after amplification. The two quantities were measured in different instants of time, in which the configuration has to be changed manually. Despite this, the V_{OC}, I_{SC} and load sweep acquisition were performed automatically, controlled by a matlab script. The oscilloscope was connected to a computer, using VISA communication

standard [23, 27], where the data was immediately acquired and displayed in a matlab plot. Also, using a matlab script the arduino nano, connected to the digital potentiometer, was controlled and in a very automated mode, the load sweep was performed.

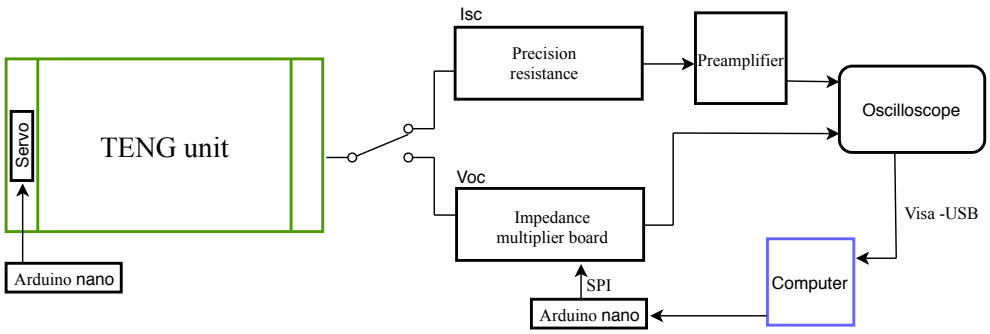

Figure 4.6: Setup diagram.

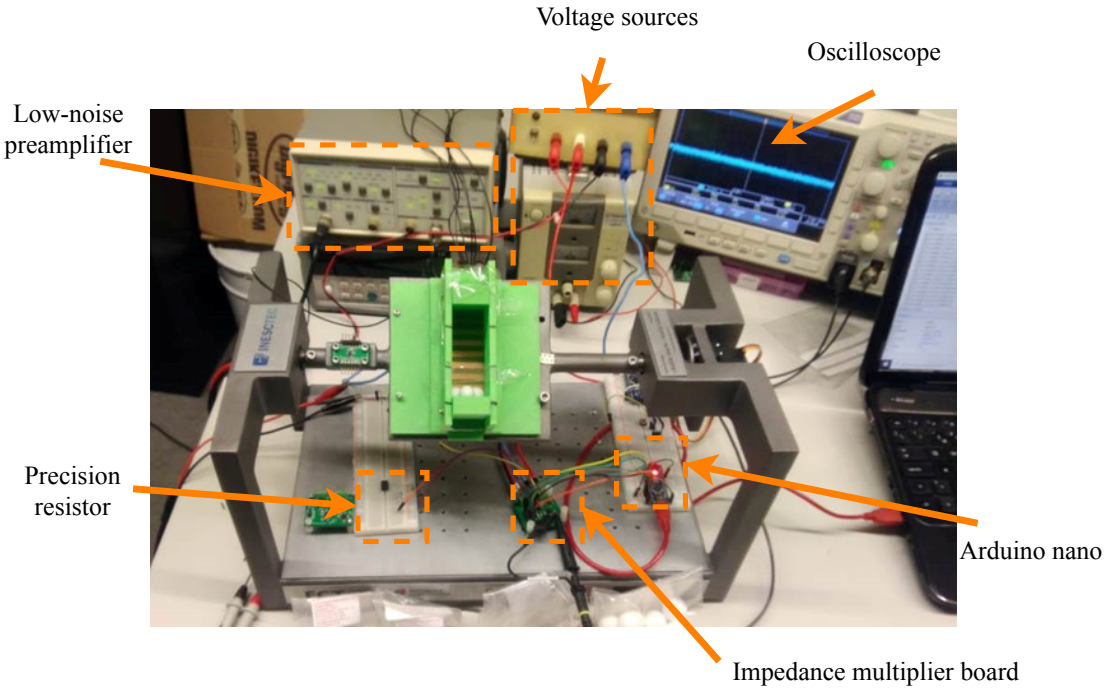

Figure 4.7: Measuring equipment.

Thus, in this section was presented all the devices that have been used to measure the electric output parameters of the proposed TENG. In Figure 4.7. is shown the setup mounted with all the equipment used to characterize, in an automated manner the TENG. In addition to the devices already presented, two power supplies were used: one to power the servo motor and the other to power to the opamp with a dual voltage($\pm 12V$).

Chapter 5

Results and Optimization

The results obtained and the optimization study to improve the electrical output of the TENG will be presented in this chapter.

After the fabrication of the proposed TENG and the creation of a systematic test process for the performance evaluation, the electric output characterization was performed. Only the characterization of the second TENG implementation proposed will be presented. To characterize the electrical output performance of the TENG, we measured the open-circuit voltage (V_{OC}) and the short-circuit current (I_{SC}).

For the proposed TENG, several studies were performed in order to achieve the optimal conditions of operation. Different materials, spheres size and a different number of spheres inside the structure were studies. Besides that, the distance between the two adjacent electrodes (d_{gap}) also was studied. Table 5.1 summarizes all the parameters that were experimentally tested to find the best condition of operation.

Tested parameters	**Values**
Distance between electrodes (d_{gap})	2.5 mm, 5 mm, 10 mm
Spheres sizes (diameter)	6.4 mm, 9.5 mm, 12 mm, 20 mm
Number of spheres in each unit (n)	1-20 (depending on the size)
Spheres Material	PTFE, Nylon 6.6, Polystyrene

Table 5.1: Parameters tested for otimization.

Figures 5.1(a) and 5.1(d) show, respectively, the V_{OC} and I_{SC} during 10 second of acquisition, with the following conditions: one PTFE sphere of 12 mm and a distance between electrodes of 9 mm. In Figure 5.1(a), each set of voltage peaks represents one movement of the sphere between each side of the box, under a controlled movement. Expanding one of these sets of peaks (Fig.5.1(b)), it is possible see five distinct peaks, in which each peak represents the successive touching of the sphere between adjacent electrodes, depicted in Fig.5.1(c).

In these conditions a maximum peak voltage of 3.5 V and a short-circuit current of 140 nA is approximately achieved. As discussed, the measurements presented here were done under the same oscillating movement, with a velocity of 60 degrees/sec. As expected, increasing or decreasing this velocity, it will only change the time distance between the set of peaks, which changes the energy produced but not the maximum V_{OC} and I_{SC}.

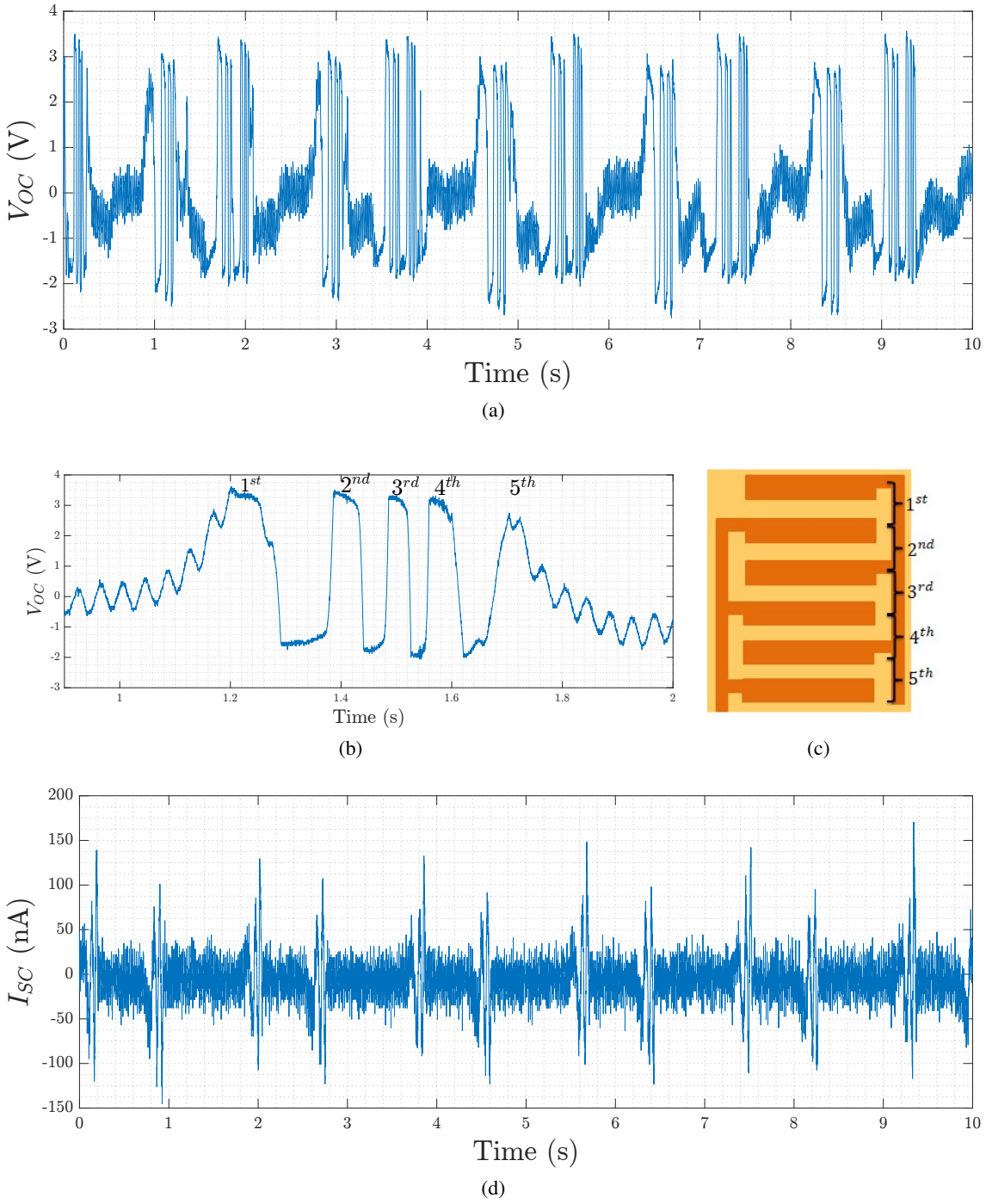

Figure 5.1: (a) V_{oc}, (d) I_{SC} and (b) voltage pulse train when one ball alternately touches (c) the electrodes.

As refereed, several types of optimization were experimentally performed to improve the electrical output of the device. Figure 5.2 shows the absolute value of V_{OC} and I_{SC} for different number of spheres ($n = 1,4,5,6,7$), when PTFE spheres with 12 mm of diameter and a d_{gap} of 10 mm were used. It is possible to conclude that the performance slightly changes with a different number of spheres, and there are an optimum number of it. With five spheres a maximum $|V_{OC}|$ of approximately 4 V and a maximum $|I_{SC}|$ of 240 nA is achieved. Above this limit, with 6 and 7 spheres, both $|V_{OC}|$ and $|I_{SC}|$ slight decrease. The reason for such behavior is that, with a large n, the free space available for sphere movement decreases, with some spheres not touching all electrode strips, decreasing the charge transference.

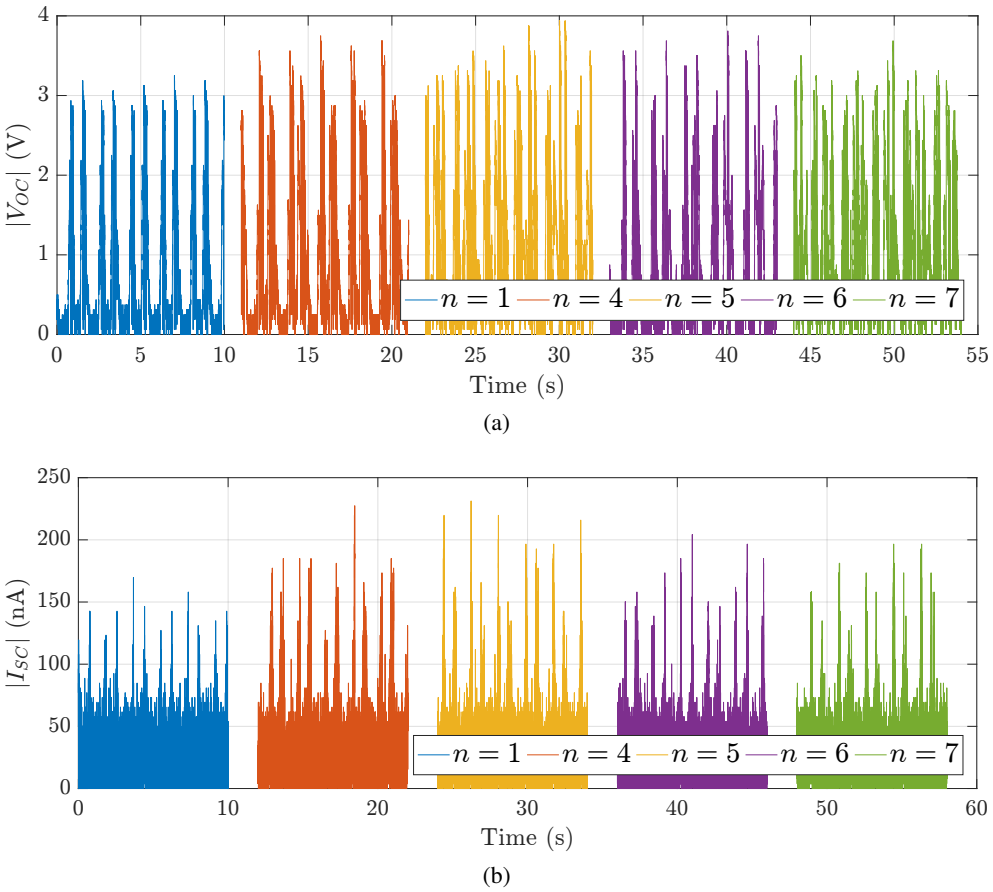

Figure 5.2: (a) $|V_{OC}|$ and (b) $|I_{SC}|$ for different number of spheres (n).

5.1 Distance between electrodes, size and number of spheres optimization

To systematically find the best parameters of operation, for each distance d_{gap} were changed the size of spheres, and in each size was changed the number of spheres (n) inside the structure. Furthermore, to best compare the performance of each parameter, the criterion used was the transferred charge in a certain period of time, under a short circuit condition (Q_{SC}). The transferred charge was calculated by the integral of the current during the acquisition time (10 s).

Figures 5.3 - 5.6 show the comparison of the transferred charge under different conditions, in which each plot shows the variations of the number of spheres and the distance d_{gap}, when the sphere size is fixed.

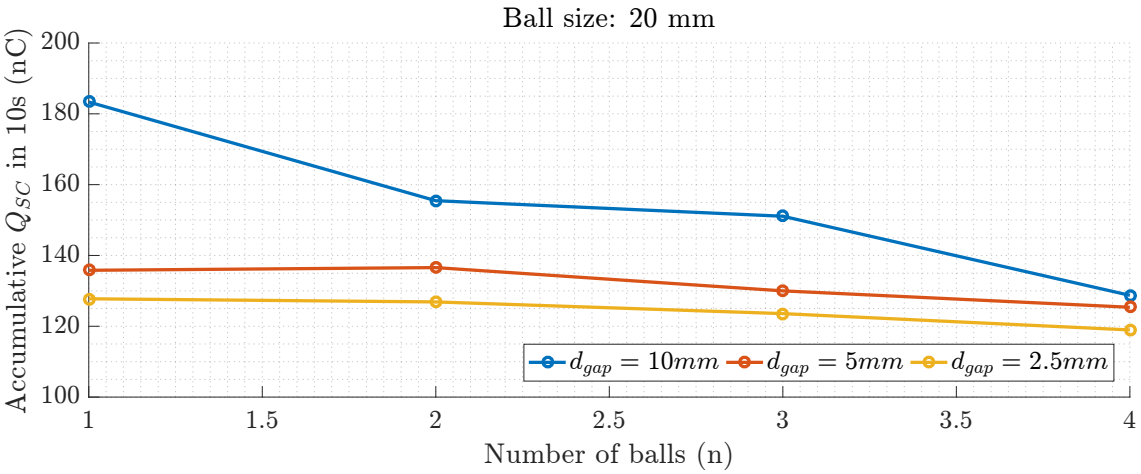

Figure 5.3: Accumulative induced charges for different number of spheres and d_{gap} distances, when spheres of 20mm were used.

When spheres of 20mm were used (Fig. 5.3), the maximum transferred charge occurred for a d_{gap} of 10 mm with only one ball, in which an approximately 180 nC of charges was transferred. With a higher number of spheres, the performance decreased and the reason for that, is again that with a large n the free space available for spheres movement decreases. Besides that, for a lower d_{gap} the charge transferred also decreases, and the reason for such behavior is that for others d_{gap}, spacing 5 mm and 2.5 mm, the sphere of 20 mm of diameter it is too large, touching at the same time two adjacent electrodes.

On the other hand, for spheres of 12 mm (Fig.5.4), two different maximum points were obtained: for five spheres with a d_{gap} of 10 mm or for eight spheres with a d_{gap} of 5 mm, in which at both cases 250 nC of charges was transferred. With this behavior, it can be concluded that with a lower d_{gap} the optimum number of spheres is shifted and to achieve the optimum point, more spheres have to be used. Although with more spheres the free space is lower, now with a lower d_{gap}, a smaller movement of a certain sphere can be enough to induce the charge transference.

We are limited by the number of spheres available for test, but following the same trend, it is expected that with a d_{gap} of 2.5 mm the optimum number of spheres will occur for a larger value

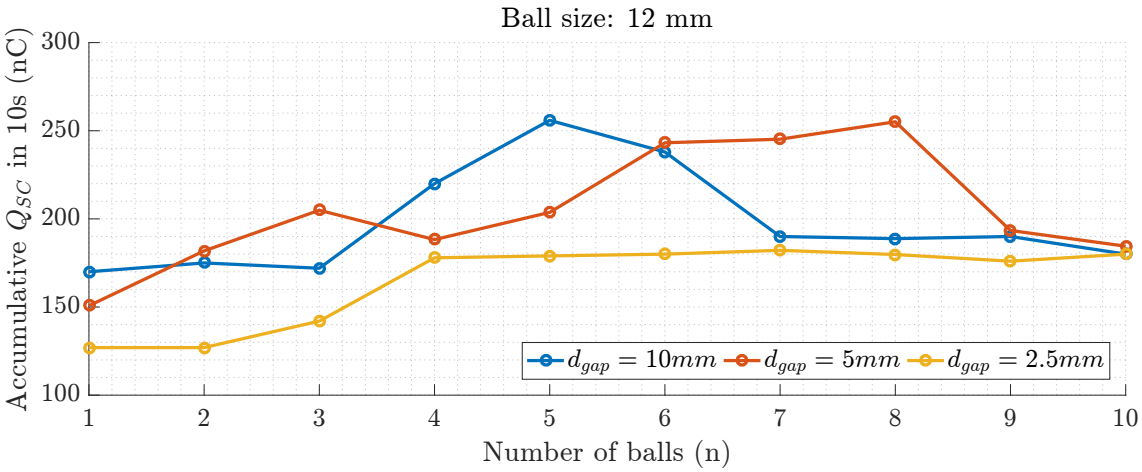

Figure 5.4: Accumulative induced charges for different number of spheres and d_{gap} distances, when spheres of 12mm were used.

of n that in the other distances, if the effect of a lower free space available does not overlap to this.

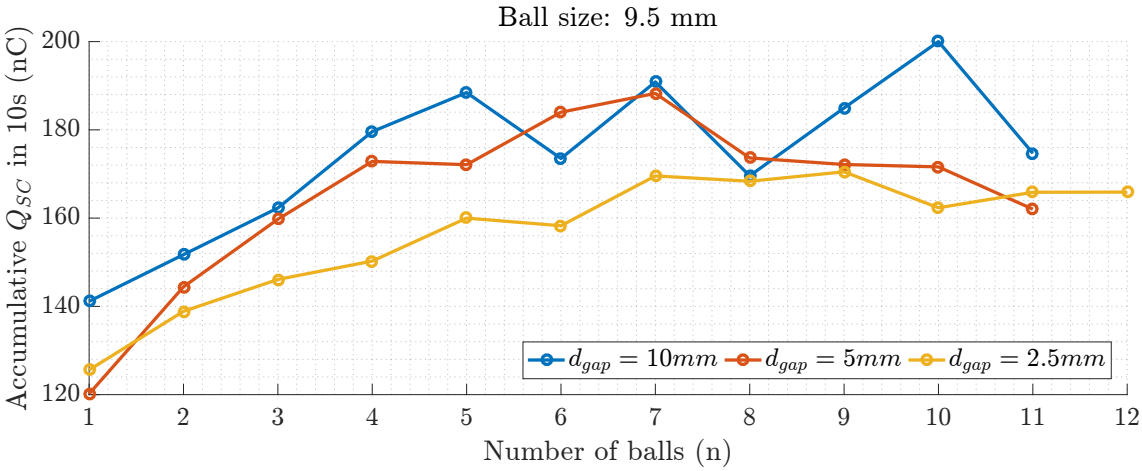

Figure 5.5: Accumulative induced charges for different number of spheres and d_{gap} distances, when spheres of 9.5mm were used.

Figure 5.5 show the situation for spheres of 9.5mm, and in is case lower results were obtained. The reason for that is that, with this size for the spheres (multiple of the width of the box), normally they get stuck between the walls of the box, not rolling during the oscillating movement. So, the results obtained for this size does not represent the real behavior in increasing the number of spheres with different d_{gap}. Another box width size should have been used to avoid this situation.

For a sphere size of 6.4 mm (Fig.5.6) the best results were obtained for a d_{gap} of 5 mm with 8 spheres, and for a d_{gap} of 2.5 mm with 12 spheres. Here a approximately 250 nC of transferred charge was achieved.

Therefore, it is easily concluded that the parameters tested change the performance of the proposed device and several conclusions can be taken. Fixing the number and size of spheres (5 spheres of 12 mm), performance is increased for lowers d_{gap} distances (Fig.5.8). Besides that, for

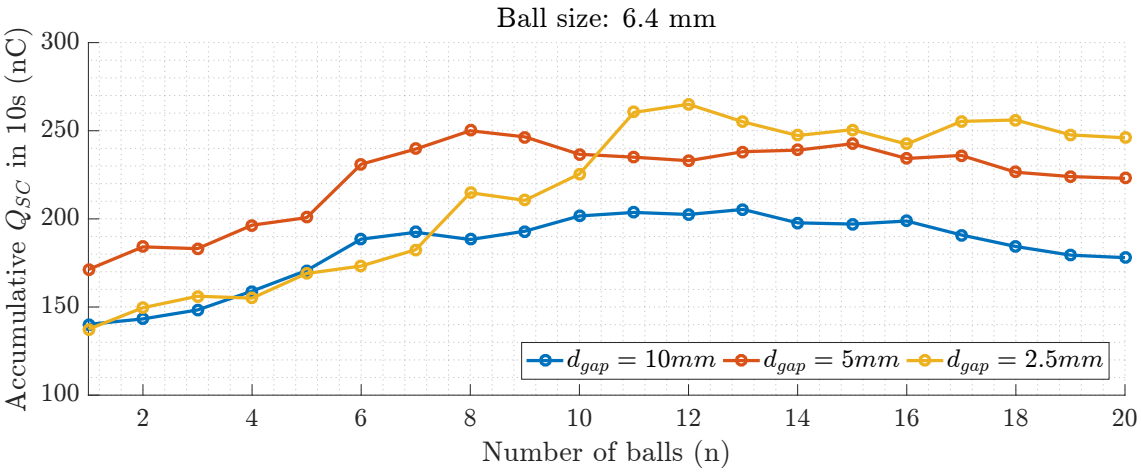

Figure 5.6: Accumulative induced charges for different number of spheres and d_{gap} distances, when spheres of 6.4mm were used.

each d_{gap}, there is an optimum number of spheres that maximize the accumulative charge but that depends on the diameter of the spheres.

Several optimal points were found, but only one was chosen for the final implementation. We fixed a d_{gap} of 2.5 mm and an optimum number of 12 spheres, with 6.4 mm of diameter that was used for the following measurements.

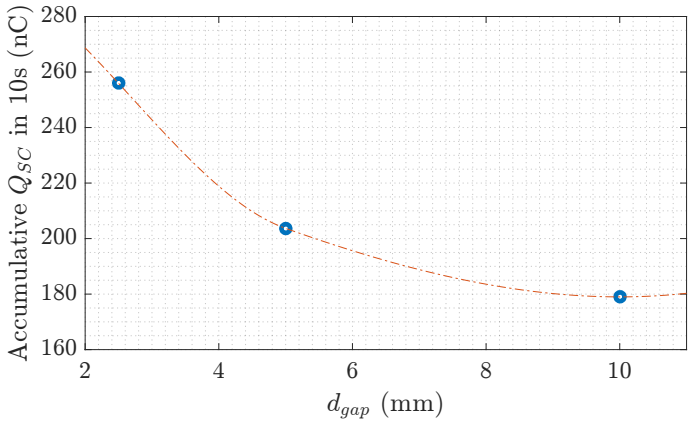

Figure 5.7: Accumulative induced charges for different d_{gap} distances (for 5 spheres of 12 mm) .

5.2 Material influence

The previous results showed, were all realized with spheres of PTFE. This material was what showed the best results, as can be seen in Figure 5.8, where the sphere's materia was changed, keeping fixed the other parameters (d_{gap} of 10 mm and 5 spheres of 12 mm). For spheres of Nylon and polystyrene $|V_{OC}|$ and $|I_{SC}|$ were significantly lower. However, based on the triboelectric

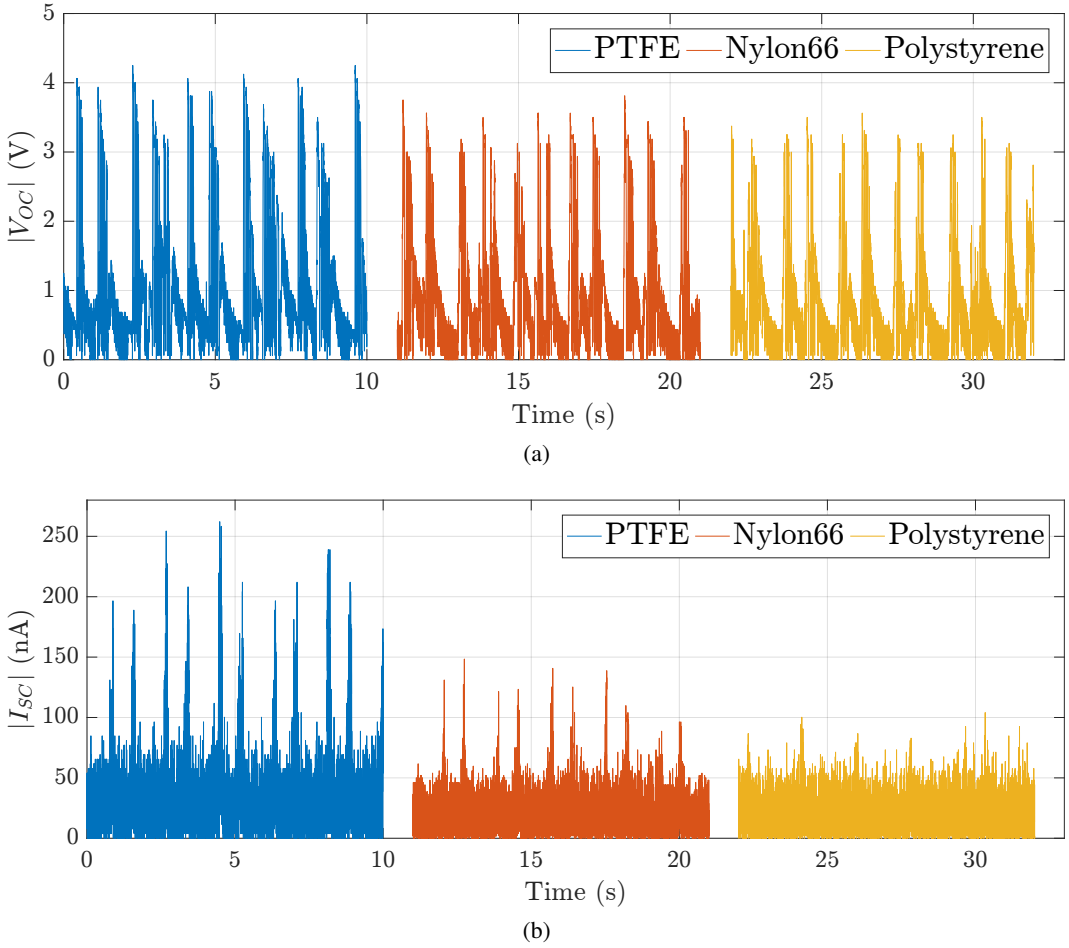

Figure 5.8: (a) $|V_{OC}|$ and (b) $|I_{SC}|$ for different materials, fixing the same d_{gap}, n and spheres size.

series, presented in chapter 2, this result was unexpected. As mentioned, to improve the triboelectrification the materials should have the most opposite triboelectric polarities, which means that should be used the farthest materials presented on the triboelectric series.

So, comparing in Table 2.1 the position of the PDMS (material applied in PCB) with the materials used for the spheres, it is easily concluded that PTFE should lead to the worst results and the Nylon the best electrical outputs, which experimental did not happen. Although we are not able to explain with certainty this behavior, we believe that some contamination occurs on the surface of the spheres or on the surface of the PDMS film during the fabrication process. However, the material chosen was PTFE, and the test of the other parameters was realized with this material, as already showed.

5.3 Power characterization

After finding the best physical parameters that maximize the electrical outputs of the proposed device, having as a criterion the open-circuit voltage and the short-circuit current, load characterization was also performed in order to find the load resistance that maximizes the energy produced.

Figure 5.10(a) shows the average output power for different external load resistances, where the resistance was changed between 1 kΩ to 1.4 GΩ, using the developed board presented in Figure 3.4. Maximum output power of approximately 30 nW for a load of 35 MΩ was founded. With these results, one can state that problems of mismatch between TENG and any energy storage units will occur, because TENGs have inherently high impedance while energy storage devices such as batteries and capacitors usually have low impedance [28]. This problem will be discussed in the next chapter.

Figure 5.10(b) shows the trend for maximum voltage with increasing load resistance (maximum peak obtained in the voltage spikes versus time plot). Above the optimum load resistance (providing maximum output power) this voltage tends to settle at the V_{OC} value. The current follows the opposite trend, but it is not presented because of measurement difficulties. With high resistances, the current becomes much small making it impossible to measure.

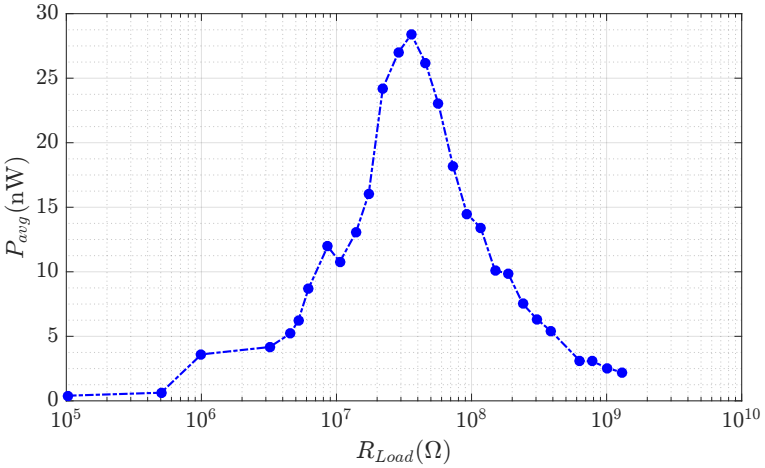

Figure 5.9: Average output power dependence for different external load resistances.

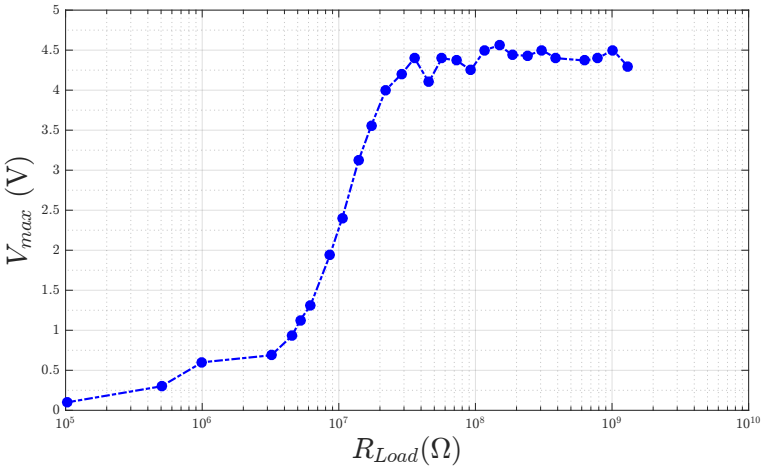

Figure 5.10: Maximum voltage dependence for different external load resistances.

5.4 Number of units

With the objective to study the scalability of the device proposed, we performed the characterization of the electrical outputs for several numbers of units (m). With the objective to increase the current generated, three units were connected in parallel, as shown in Fig. 5.12. Figure 5.11 shows the $|V_{OC}|$ and $|I_{SC}|$ for different number of units (m=1,2,3). As expected, the $|V_{OC}|$ remains constant and the $|I_{SC}|$ increases almost linearly with the increasing number of units, in which this increasing is almost proportional (Fig. 5.12(b)). With three units connected in parallel, a maximum $|I_{SC}|$ of 500nA was achieved.

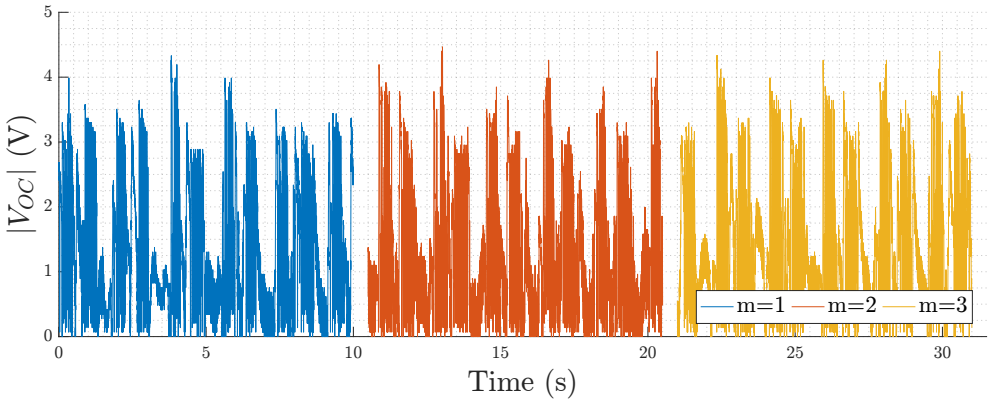

(a)

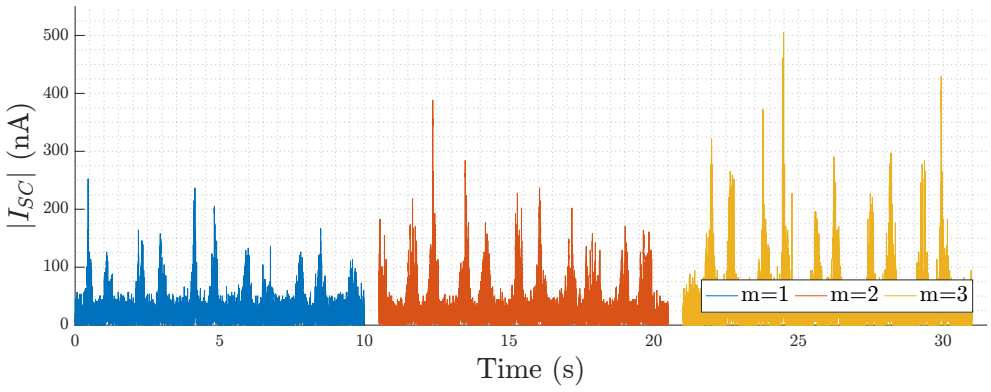

(b)

Figure 5.11: (a) $|V_{OC}|$ and (b) $|I_{SC}|$ for different number (m) of units.

5.5 Discussion

In this chapter, the design of the proposed triboelectric nanogenerator was systematically investigated. The several optimizations done allow us to conclude which are the physical parameters (distance between electrodes, size and number of spheres on the structure) that improve the performance of the device. Also investigated what are the best load conditions and what occurs in prototype performance with the increase in the number of units. An optimum load of 35 MΩ

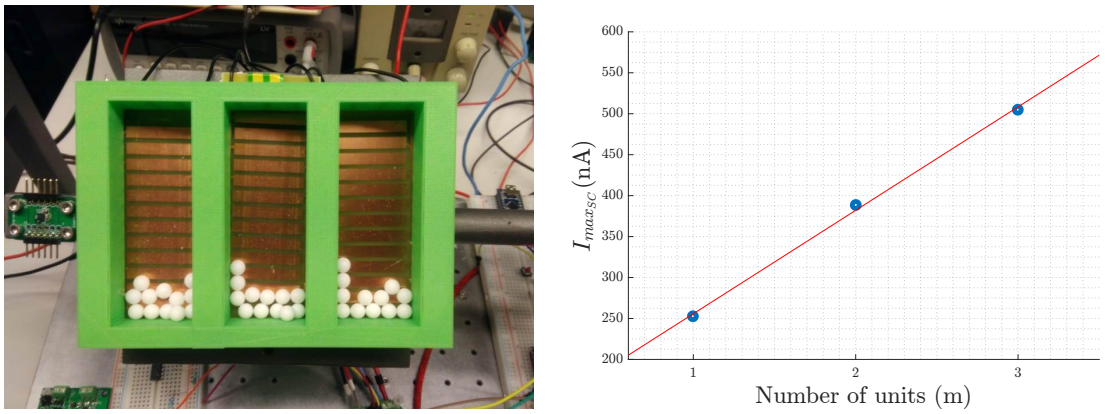

(a) (b)

Figure 5.12: (a) Photography of the structure used with 3 units attached in parallel and (b) the plot of I_{SCmax} for different number of units.

is achieved and was concluded that the performance increase almost proportionally with the number of units, in which an average output power of 30nW was reached with only one unit, which represents a power density of $12.5\,\mu W/m^2$.

Despite this, the results were not so good as expected. Compared with other similar implementations, presented in chapter 1, the output power density of the presented device was more than one thousand times lower. However, in these similar implementations sometimes it is not clear what was the implementation area that was considered to perform the power density calculation. In our case, an area of $8\,cm \times 3\,cm$ (area of the PCB) was considered.

Comparing the I_{SC} and V_{OC} of the Tower-like triboelectric nanogenerator implementation (see Fig. 1.4) [11], where with only one unit a maximum short-circuit current of $1.3\,\mu A$ and an open-circuit voltage of $105\,V$ was reached, with our implementation, the results of our TENG are smaller. Some reasons can be pointed out as the cause of this performance results that were obtained for this device. Firstly, the unexpected behavior of materials, in which the best electrical results occurred with the theoretical worst materials, leading us to conclude that some type of contamination occurs on the materials. Secondly, in all the presented devices, nanowire-like structures were built on the surface of one of the triboelectric layers to enhance the contact area and improve the electrical output, but, in our device this treatment was not performed. Thirdly, the error of measurement could have degraded the results. As explained, the current results were taken by measure the drop voltage in a resistance of $100\,\Omega$ and after that the signal was amplified by a low noise amplifier. The probes parasitic effects could have degraded the results.

Chapter 6

Power management strategy for TENG

After developing an optimized implementation that surely can harvest energy from random environments, a new question arises. How the TENG can be used to power electronic systems for practical applications?

To embed TENGs into an electronic system, there are major challenges to overcome. First, due to the randomness of the mechanical energy source and the intrinsic capacitive behavioral of TENG, makes that the output signal is normally in the form of a pulsed ac signal [28]. Secondly, TENG has a high inherent impedance of typically in several Mega ohms level with high voltage of typically tens or hundreds of volts and low current (typically).

These characteristics lead to low energy transfer efficiency for either powering electronics or charging a battery/capacitor directly since usually they have relatively low impedance. Effective power management plays an essential role in efficient energy utilization of TENG, which has always been the difficulty and bottleneck for the practicability of TENG [29]. Traditionally, a bridge rectifier is used to convert the ac to dc and then the energy is directly stored into a large capacitor (direct charging method) [28]. However, normally the impedance mismatch results in an ultra-low energy storage efficiency of only 1%, according to the authors in [28].

Most of the research in TENGs mainly focus only on output performance under external load resistances and few papers explore the process of using a TENG to charge an energy storage unit. In this chapter, based on some of the power strategy already presented in the literature, will be presented and simulated a strategy for power management, that could be applied to the device developed or to another TENG implementation.

6.1 Theoretical Simulation of a TENG

To design a power management strategy for triboelectric nanogenerator, the circuit model of a TENG mode demonstrated in chapter 2 will be used to simulate the real-time output characteristics of a TENG. Based on the lateral sliding-mode circuit model, deduced in chapter 2, was embed on an electrical simulator, to perform the study of a power management strategy. This design flow was already proposed and validated in [15, 30]. The mode chosen to perform this simulation does

not represent the proposed device, it only was chosen because of the simplicity of the equations, facilitating the study of a power management strategy. The conclusion obtained can be generalized for other types of modes and motions [15].

To perform the simulation of a sliding-mode TENG, the circuit model (see equation 2.13 and 2.12) was introduced on the Cadence Virtuoso simulation tool using a Verilog-A script [31], to easily define a variable capacitor and a voltage source, both dependent of the motion. A typical motion used on TENG simulation is a mechanical harmonic motion, that also was used in our simulation, in which $x(t)$ is defined as [15]:

$$x(t) = x_{max}[\frac{1}{2} - \frac{1}{2}cos(\frac{\pi v}{x_{max}}t)] \tag{6.1}$$

Also to perform this simulation the parameters of materials and the motion was to be defined. Table 6.1 list the parameters used in this simulation that are the same parameters presented in [28], in which a lateral sliding mode was also simulated. The time-domain results obtained were compared and validated with the results presented in [15].

Parameters	**Sliding-mode TENG**
Dielectric effective thickness, $do = \sum d_1/\varepsilon_1 + d_2/\varepsilon_2$	90.8 mm
Width of dielectrics W	8.5 cm
Length of dielectrics L	7.9 cm
Tribo-charge surface density σ	-12uCm^-2
Maximum displacement, xmax	3.5 cm
Velocity v	1 ms^-1

Table 6.1: Parameters of the TENG used for simulation.

The real-time voltage from the simulator for a specific load value of 10 MΩ under a periodic motion is plotted in Figure 6.1. The behavior of voltage, current and power were experimentally obtained for this simulated TENG under different external load resistance, depicted in Figures 6.2, in which the maximum output power of approximately 20 µW is obtained for a load of 30 MΩ.

Another way to represent the energy output of TENG is through the plot of built up Voltage (V) against the transferred charges (Q). Figure 6.3 shows the relation between the voltage and the charge transferred (accumulative integral of current) during a cycle of movement. Once the signal of TENG is periodic, as seen in figure 6.1 in responding to the periodic mechanical motion, the V-Q plot is a closed-loop. As we can see, with different external loads the shape and the area of the loop is different. Based on the equation 6.2 [22], which gives the energy (E) produced in a certain period of time (T), it is easily concluded that the encircled area of each closed-loop, represents the

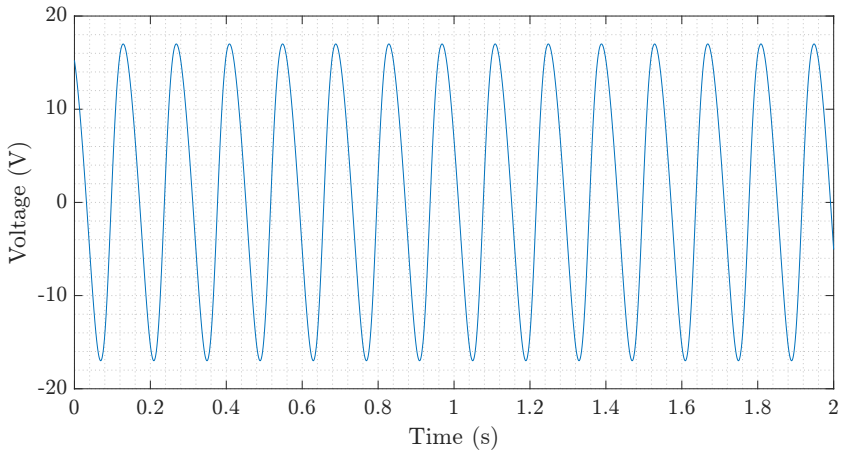

Figure 6.1: Voltage output under a load of 10MΩ.

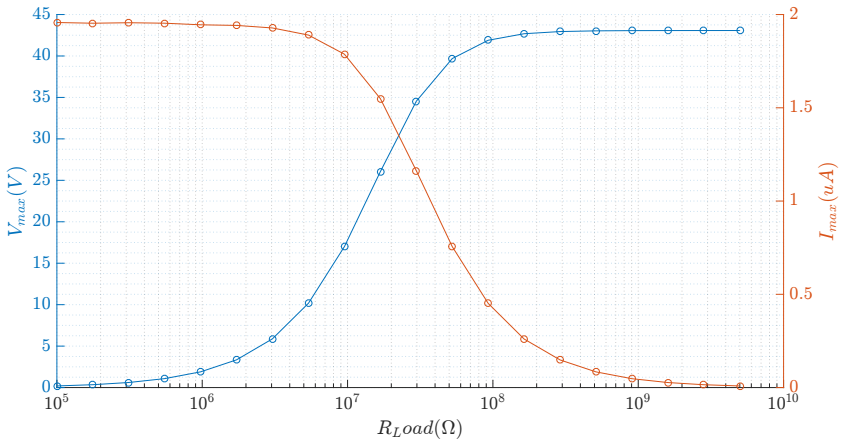

(a)

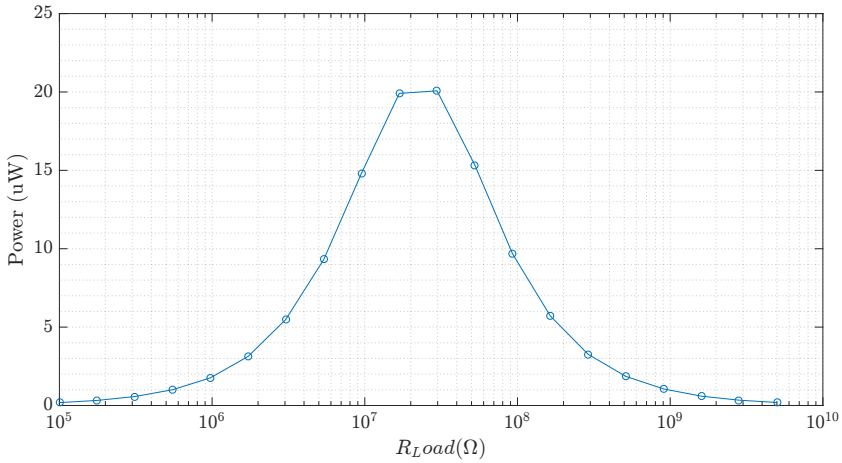

(b)

Figure 6.2: (a) Maximum voltage (V_{max}) and maximum current (I_{max}). (b) Average output power(b) for different external load resistances.

energy transferred per cycle.

$$E = PT = \int_{T}^{0} VIdt = \int_{t=T}^{t=t} VdQ = \oint V\,dQ \tag{6.2}$$

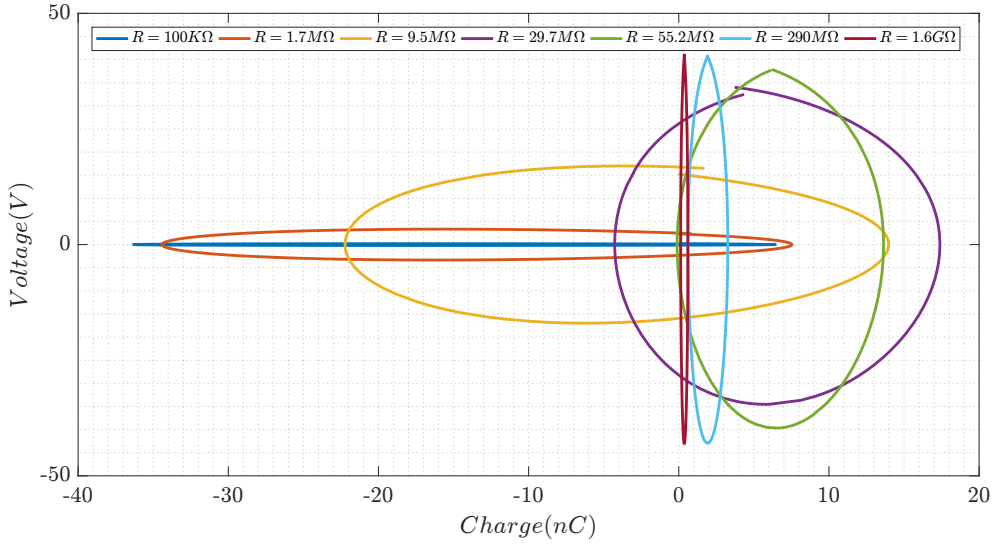

Figure 6.3: Voltage (V) and charge transferred (Q) relation per cycle for different external load resistances.

Once again, is possible to see that the maximum energy produced per cycle is obtained with a load resistance of approximately 30 MΩ. Another conclusion, taken by this plot, is when the load is lower than 100kΩ and higher than 1.6GΩ we have, respectively, the maximum transferred charges (Q_{max} - width of the circle) and the maximum voltage (V_{max} - height of the circle). In other words, bellow an above these loads limits we approach the condition of short-circuit and open-circuit, respectively.

6.2 Maximizing the output energy of a TENG

We can note that the maximum transferred charges (Q_{max}) occur on the short-circuit condition and by opposition, the maximum voltage (V_{max}) happen on the open-circuit condition, and so this two conditions occurs with extreme loads ($R_L = 0$ and $R_L = \infty$). Therefore, a maximum energy output state is never reached. Until now, experimentality or simulated, we only were able to find the load that gives us the maximum output energy, but it is not the maximum energy output state. If we could obtain the $V_{oc_{max}}$ at low resistances or the $Q_{sc_{max}}$ at high resistances, in order to ensure that V_{OC} and I_{IC} occurs at the same load, the state of maximum energy output could be obtained.

Using a switch implementation that changes the load between the two stages (SC condition and OC condition), ensuring the $V_{oc_{max}}$ and $Q_{sc_{max}}$, maximum energy could be obtained [22,32]. To better understand this concept, a simulation was performed where an ideal switch was connected in series with the TENG and a load of 1 Ω (to represent a short-circuit) (Fig.6.4(a)). When the output voltage reaches an imposed voltage threshold (near to $V_{oc_{max}}$) the switch became on and the TENG is connected to the load. The operation for this serial switch works as shown in Figure 6.4(b) and can be divided in the following steps: Step I, the switch is off and the voltage change at reach to the voltage threshold (43V); Step II turn the switch on to enable current flow to load and then turn the switch off; Step III the switch is off and the absolute voltage change at reach again to the

voltage threshold; Step IV turn again the switch on to enable current flow. Figure 6.5 show the time-domain voltage and current where is possible to see that when the switch turn on a current peak occurs and the voltage goes to zero, as expected. The switch was controlled by a Verilog-A script on Virtuoso software, that after sense the TENG maximum voltage, generates a pulse signal to close the switch.

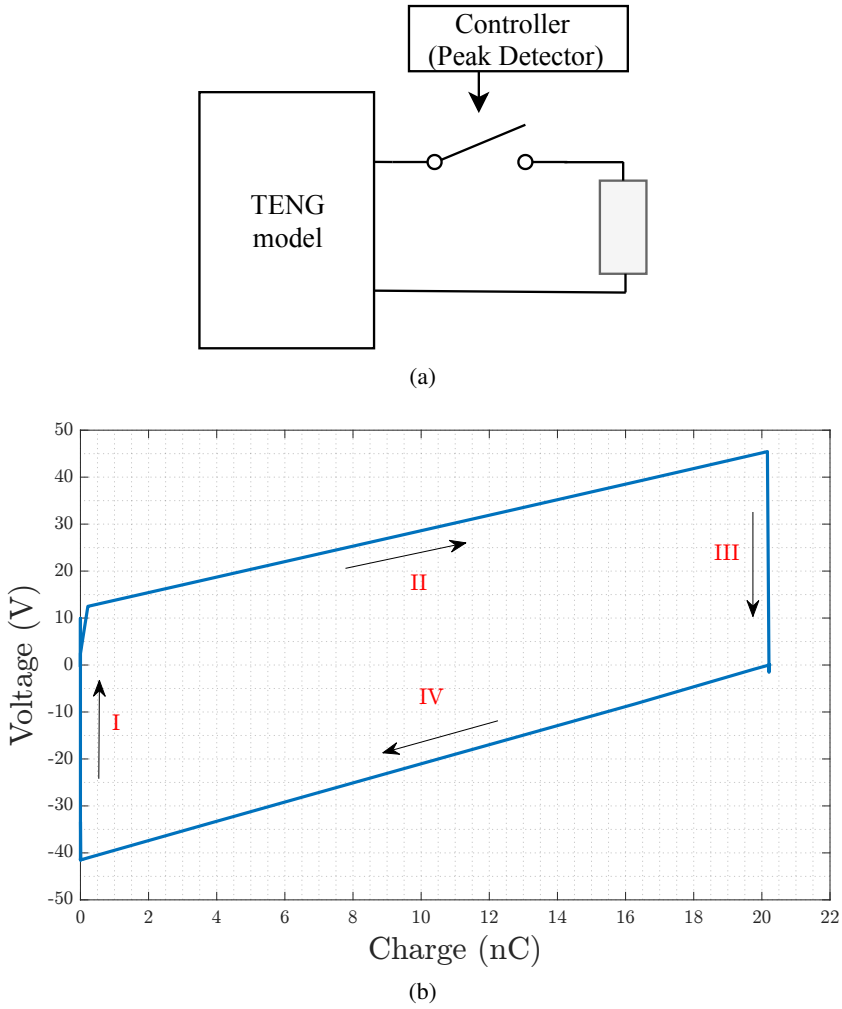

Figure 6.4: Simulated switched circuit. (a) Schematic diagram when a switch is connected in series and (b) V-Q relation using a load of 1Ω.

Comparing the area of the simulated V-Q plot when a load of 30 MΩ is used with this last implementation (switched circuit), increased energy from 809.74 nJ to 1 µJ per cycle is achieved, what represents an improvement of 19% on the energy produced per cycle.

Figure 6.6 shows the V-Q plot when a circuit switched is used, but now with different load resistances. It is possible to conclude that with a higher load the energy produced is lower because now, the Q_{max} state that occurs in a short-circuit condition is not achieved. Table 6.2 shows the energy produced per cycle with different loads. Once again, is possible to see that with this strategy is possible to extract more energy of a TENG than with an optimum load. However,

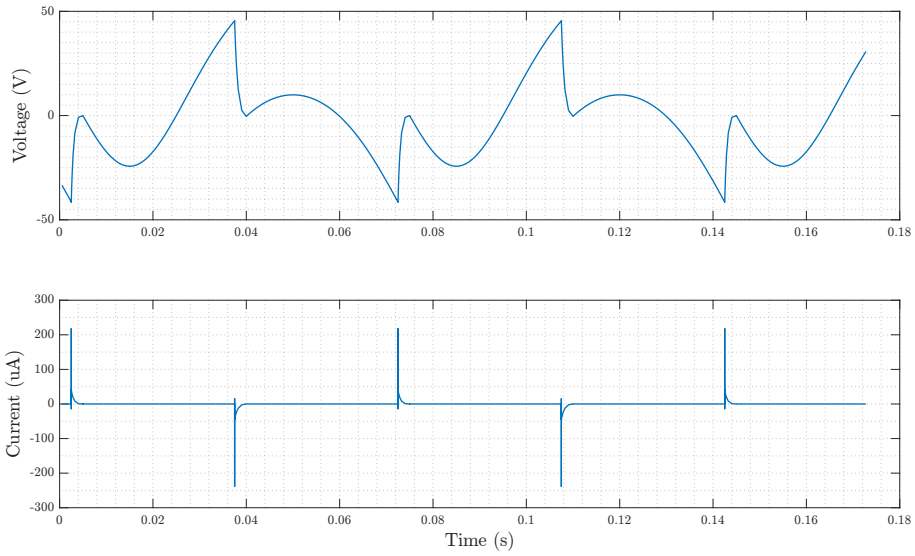

Figure 6.5: Simulated time-domain (a) voltage and (b) current with a switched circuit.

above a certain limit (approximately 100 kΩ) the performance became the same that with a load of 30 MΩ,the moment in which the advantage of using a switched circuit is lost.

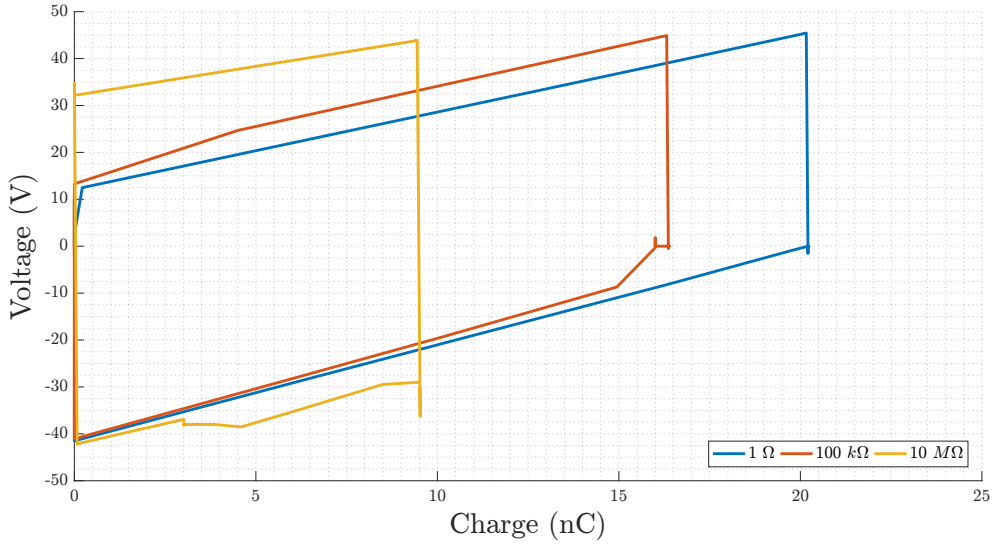

Figure 6.6: V-Q relation for different loads.

The implementation presented, allow us to achieve the maximum energy output of a TENG, called “cycles for maximized energy output” (CMEO) state [22], by changing the output load between an open-circuit state and a low resistance. The complementary circuit in which a switch is connected in parallel with the external load (Fig.6.7(a)), also allows achieve the CMEO state. However now, a high load resistance has to be used to reach this state. Figure 6.7(b) shows an ideal switch connected in parallel with a load of 10 GΩ. As seen by the plot in Fig.6.7(b), the result when a switch in parallel is used, is similar to the previous result with a serial-switch design. The only difference is that now the energy is maximized with a high load, ideally infinite ($R_L = \infty$).

Load	Energy produced
30 MΩ $(withoutswitch)$	809.74 nJ
1 Ω	1 µJ
100 KΩ	876 nJ
10 MΩ	698.8 nJ

Table 6.2: Energy produced per cyle under different load conditions.

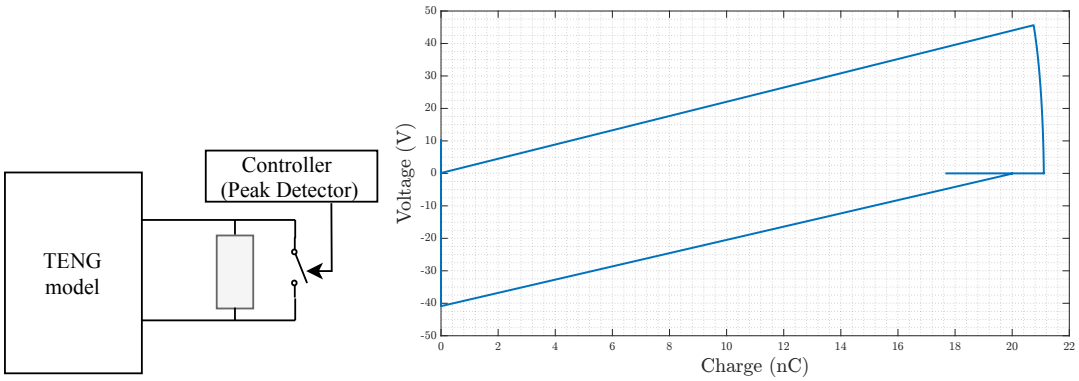

(a) (b)

Figure 6.7: Simulated switched circuit. (a) Schematic diagram when a switch is connected in parallel and (b) V-Q relation using a load of 10GΩ.

Although the results with the two configurations could be similar, using a switch connected in parallel increases the effective impedance of TENG what hinders the design of a power management system [33]. Due to this, was adopted a serial-switch design on the proposed power management that will be presented, allowing obtain the maximum energy output at a lower resistance.

6.3 Power management

As already presented, the energy withdrawal of a TENG can be maximized, however, the pulse generated still cannot directly supply any electronic device. An ac to dc conversion and managed have to be performed to enable the energy storage in an external unit.

Recently, some management strategies for transferring the maximized energy output of TENG to an external storage had already been presented in the literature. For example, in [29] a direct current (DC) buck conversion and a self-management mechanism was proposed. In this implementation, a full-bridge rectifier is used to convert the signal to a dc domain and after that, a buck converter is used to step-down the voltage, as depicted in Figure 6.8(a). The switch is used not only for the DC buck conversion but also to maximize the energy transferred as discussed above.

To achieve an autonomous switching by the TENG the authors use a micro-power ampop in a comparator configuration and a MOSFET, that they call "Tribotronic energy extractor" (Fig. 6.8(b)). The comparator is used to compare the rectified voltage (U_T) with a preset reference voltage (U_{ref}), turning on or off the MOSFET. By presetting (U_{ref}) according to V_{max} it can be realized that the switch is autonomously turned on when the voltage of TENG reaches to the peak, maximizing the transferred energy. Comparing the energy produced using this implementation with the transferred energy with a matched resistance, an experimental efficiency of 80.4 % is reached with this switched circuit, according to the authors.

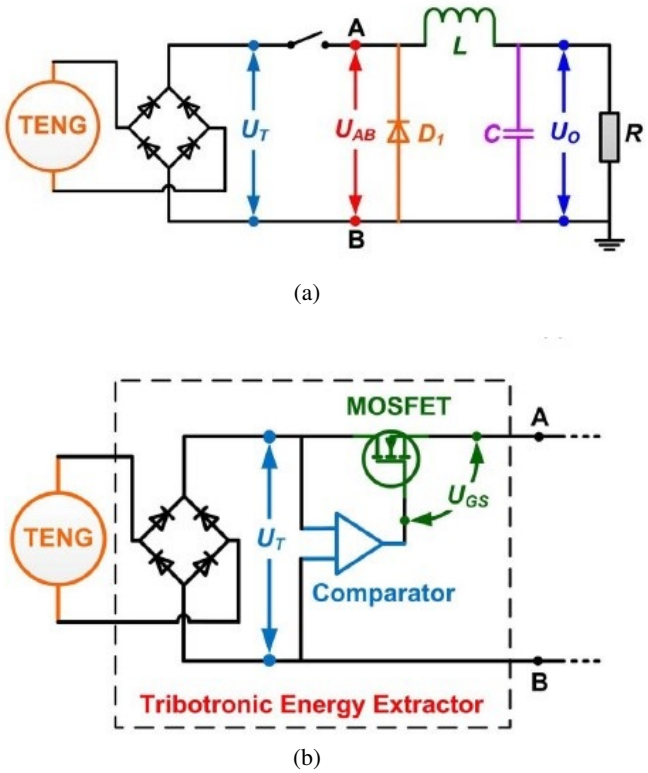

Figure 6.8: (a) Schematic circuit diagram of AC-DC buck conversion by coupling TENG, rectifier and classical DC-DC buck converter. (b) Schematic of the tribotronic energy extractor (from [29]).

In [33] another strategy was presented, also based on a switched circuit to accomplish the CMEO state. Again a full-bridge rectifier was used, connected a to a flyback converter [34] to realize a DC/DC conversion with galvanic isolation (Fig. 6.9). Once again, the switch (also controlled by a comparator topology) is used with two purposes: for the DC/DC converter and to maximize the energy transferred. Figure 6.10 shows the working mechanism of this implementation. When the switch is closed, the energy is stored in the magnetizing inductor of the transformer and when the switch is open, the energy stored in the transformer is released to the output. With this strategy, according to the authors, an experimental efficiency of 75.5 % is achieved.

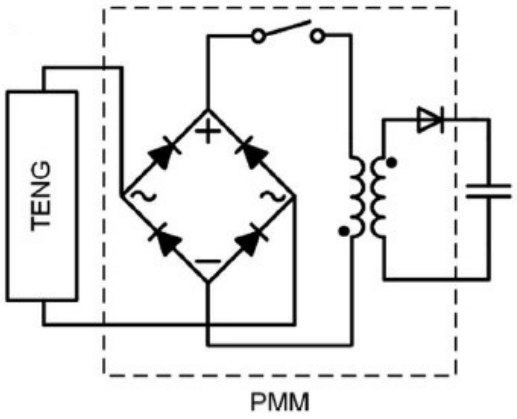

Figure 6.9: Schematic circuit diagram of the power management strategy proposed based on a flyback converter(from [33]).

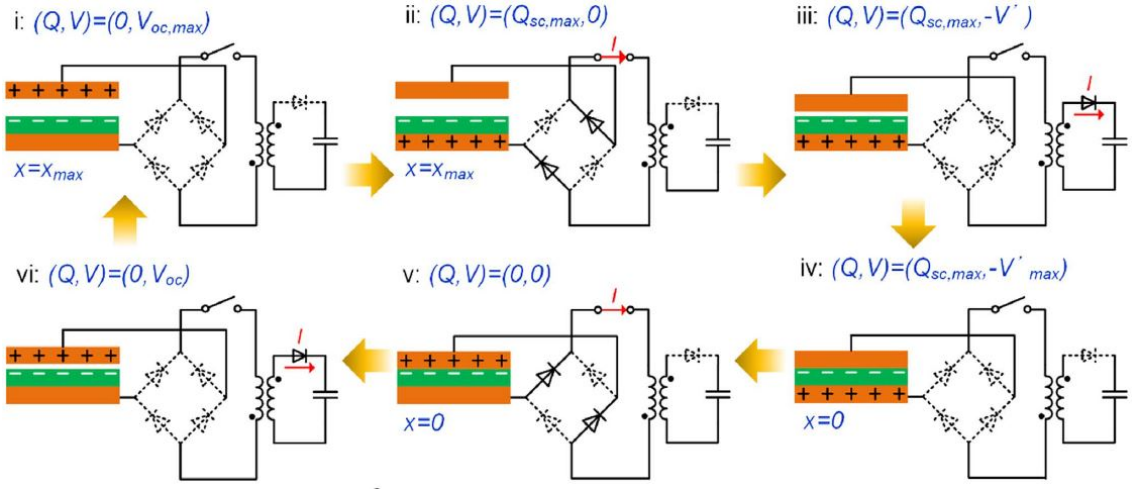

Figure 6.10: Working mechanism of the power management strategy proposed by the authors (from [33]).

6.3.1 Current-Doubler Rectifier - A New Approach

Although the two strategies presented, accomplish a good efficiency, in this dissertation project was trying to investigate another strategy for power management for TENGs. As discussed above, TENG is characterized by having a high voltage (tens or hundreds of volts) and low current (µA typically). Then, we decide to investigate by simulation a current-doubler rectifier implementation [34], that besides doing the rectification of the ac signal, perform the step-down of the voltage generated, in a very simple implementation (Fig.6.11), using only two inductors, and two rectifier diodes. Normally, this type of implementation is used in an isolated DC/DC converter, in which the current-doubler rectifier is connected to the secondary side of the transformer. However, we used a current-doubler rectifier directly, in which the TENG and a series switch is connected to this topology.

To understand the mechanism of this topology, in Figure 6.12 shows the two operation states

that allow rectifying an ac signal and doubler the current delivered to the unit storage. When the voltage applied is positive, $D2$ is forward biased and $D1$ is off, making a current path passing by $L1$ and $D2$, storing energy on the inductor $L1$. At the same time, the inductor $L2$ releases the stored energy to output through $D2$. By opposition, when the voltage applied is negative, $D1$ is forward biased and $D2$ is off, creating the current path showed in Figure 6.12, making that $L2$ store energy and the Ll releases the stored energy to output.

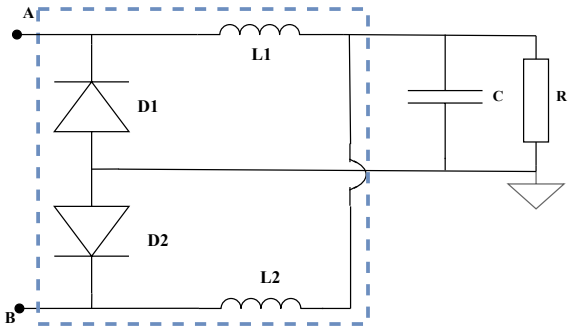

Figure 6.11: Schematic of a current-doubler rectifier topology.

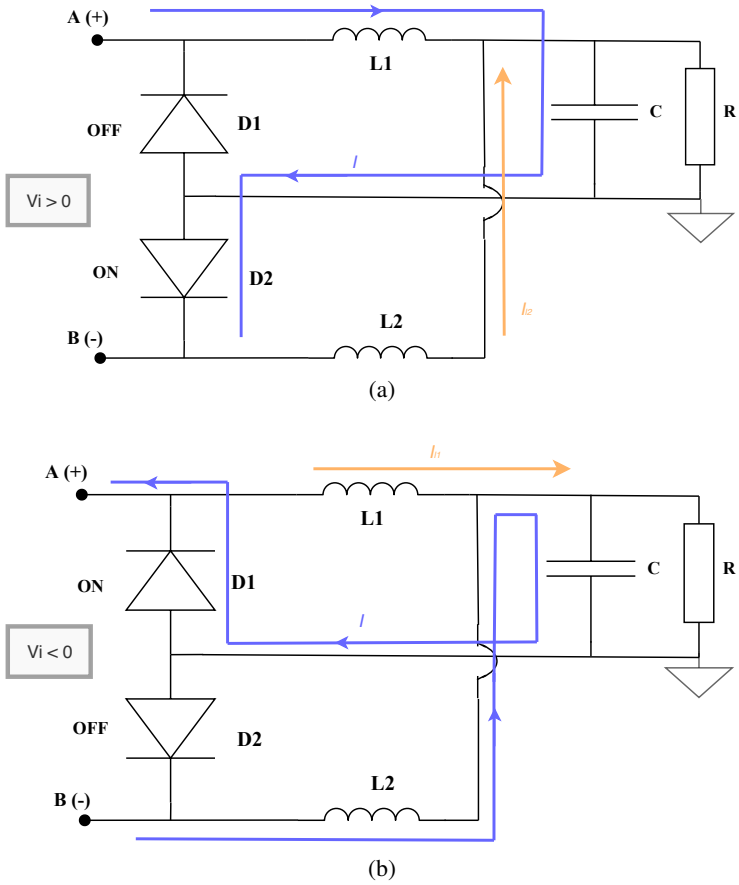

Figure 6.12: (a-b) Operation states of a current-coubler rectifier (adapted from [34]).

This implementation provides a simplified solution that makes it possible to double the current and halve the voltage (noted that is formed an inductive voltage divider), using inductors with the same value. One of the advantages of this solution is that any time just one diode is rectifying, which can improve energy efficiency because only exist the forward voltage drop on one diode, comparatively what happens in a full-bridge rectifier, where two diodes are conducting each time.

In figure 6.13 is showed the simulation voltage results when an ideal sinusoidal signal (10V of amplitude and 5Hz) is applied to the current doubler. In this simulation was used only ideal components, in which an R of 1MΩ, a C of $1uF$ and L of $1uH$ was used. By the plots of figure 6.13.(b) and 6.13(c) is seen the behavior of the inductor voltage divider of $\frac{1}{2}$ and in figure 6.13.(c) is showed the rectified signal having a DC component of nearly $5V$ and an undesirable ripple of $0.4V$. These values are dependent on the output filter capacitance (C and R) and for a bigger R, a lower ripple factor is accomplished.

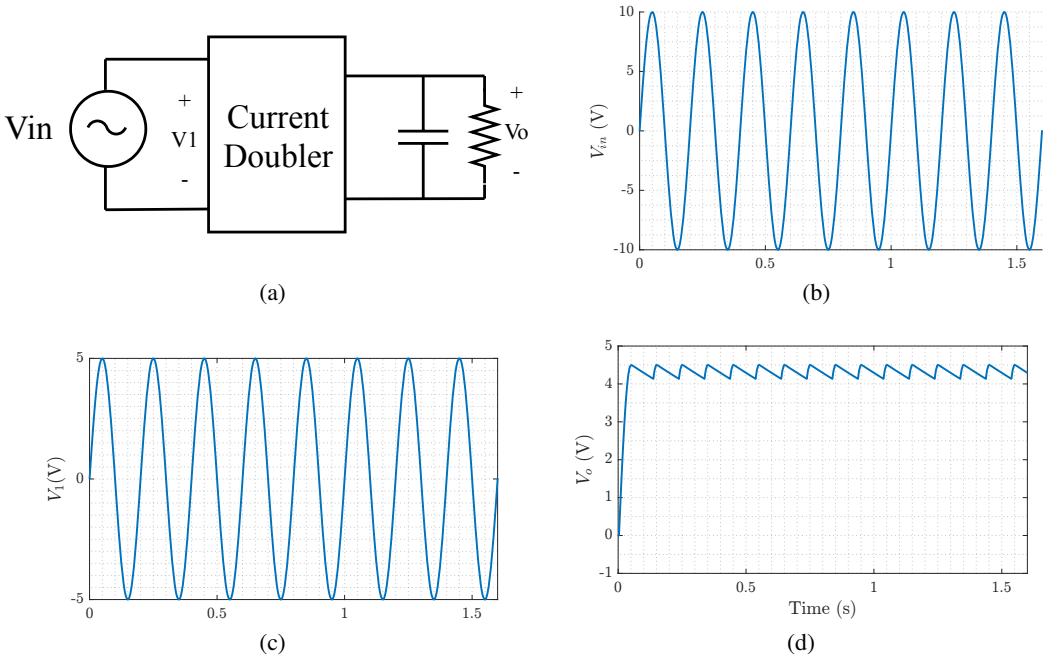

Figure 6.13: (a) Schematic of the circuit simulated. (b-d) Results of simulations.

After test the current doubler behavior and check this simple implementation, was simulated the TENG with a serial-switch and the current doubler circuit (Fig-6.14), becoming this approach a new strategy never presented for a power management TENG system. The switch used for achieving the CMEO state is controlled by an external block that when the output TENG voltage reaches a voltage threshold (near to V_{OC}) the switch became on and the TENG is connected to the current doubler. This block what behaves as a simple peak detector (also used on the above simulations) was implemented by a Verilog-A script. The ideal diodes were done with an ideal switch, connected as represented in Figure 6.15, showing the schematic of the circuit on Cadence Virtuoso software.

In Figure 6.16(a) is represented the output voltage under different load resistances (with C=1uF), showing that after a transition of several seconds a steady state is reached, in which the DC value depends on the load of the filter capacitance.

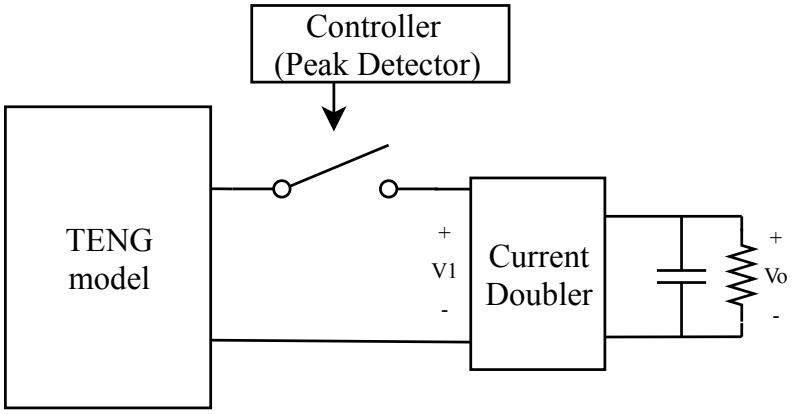

Figure 6.14: Power management strategy proposed.

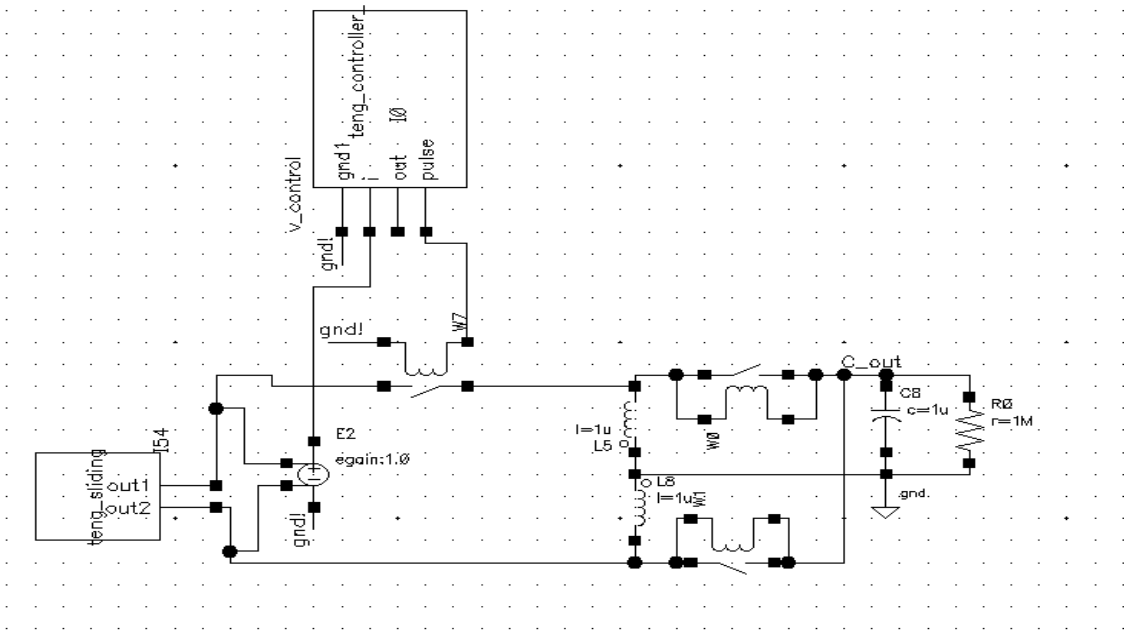

Figure 6.15: Image capture of the power management schematic under study.

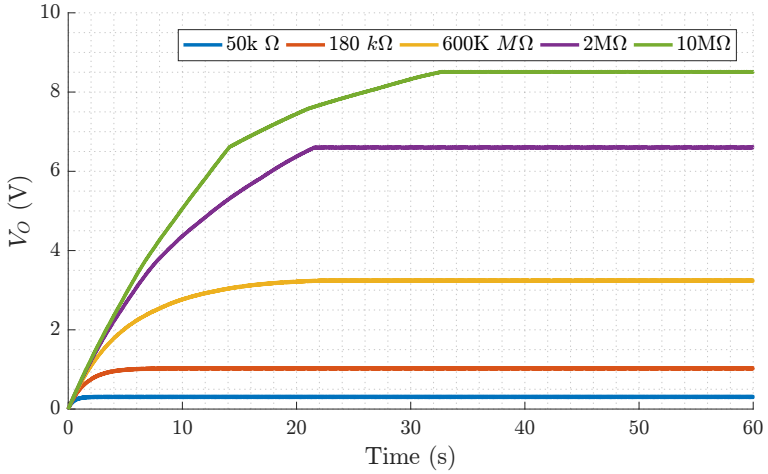

(a)

Figure 6.16: Real-time output voltage curve for different loads.

Thus, in this chapter was study by simulation, using the theoretical model of a TENG, a strategy for maximize the output energy transferred, in which a switched circuit was used. Also, it was presented a new approach of a power management module for a TENG, that could be applied to the developed device or another TENG implementation.

Chapter 7

Conclusion and Future Work

7.1 Conclusion

The triboelectric nanogenerator is an emerging technology that can be used to harvest mechanical energy from various sources of motion. TENGs have been presented as a technology with high potential due to the low cost of fabrication, high efficiency and capable of achieving high power densities.

Therefore, based on the wide range of mechanical sources that a triboelectric nanogenerator can use and on the huge amount of energy available on the ocean, recently, this technology started gaining momentum as a very promising technology for maritime applications. A TENG implementation can be used to satisfy the power requirements of small electronics systems, supporting the research and surveillance of our oceans. Some papers in this field go further and announce that this technology can be used in the future as a large-scale harvesting strategy, being a new and complementary solution to inefficient energy ocean farms that currently exist. However, to accomplish this desire a long way still needs to be covered, mostly, in the author's opinion, on materials research in order to find high longevity materials with the highest charge density possible.

In this dissertation, the main goal was to find a TENG solution that could provide the power requirements of small electronic devices, in an oceanic environment. After several experimental attempts, it has been proposed an approach relying on freestanding rolling spheres to harvest the energy from low-frequency movements. Two copper patterns have been designed and manufactured in a PCB, which act as electrodes, on the top of which a tribolectric material has been applied. The triboelectric spheres have been placed on the PCB, to move freely while touching the electrodes alternately, leading to the current flow through an external load. This implementation was tested and optimized in a controlled scenario, finding the parameters that maximize the energy output.

Despite our expectations, only a maximum output power of 30 nW was reached for each unit, representing a power density of 12.5 $\mathrm{uW/m^2}$. Inconsistent behaviors have been seen with the materials in use, which based on the triboelectric series would lead to different results from those

obtained. It is believed that the output performance obtained was strongly limited by such issues related with the materials.

Moreover, by means of a study based on simulations, a strategy has been proposed to maximize the output energy of a TENG. It has been seen that with a switched-circuit in series with the TENG, the output energy can increase approximately 19% compared to the maximum energy transferred with an optimum load. A new power management strategy, more simple than those already presented in the literature, was proposed.

Although the experimental evaluation of a TENG implementation has been realized with only three optimized units attached in parallel, in order to create a full system able to power small electronics in the ocean, a network of cells with hundreds of elements have to be used to achieve a significant power output. For example, it is here proposed a structure where hundreds of structures, each containing three TENGs units, attached to each other with different orientations, as shown in Fig.7.1(a), to harvest the energy of random movements in the ocean. This TENG network could be attached to a floating support structure, as depicted in Fig.7.1(b), to be used to charge external batteries, supplying sensors for surveillance in ocean – FLIDAR project as example, shown in Fig.7.1(c) –, in which these systems could harvest energy continuously, depending only on the maritime agitation conditions.

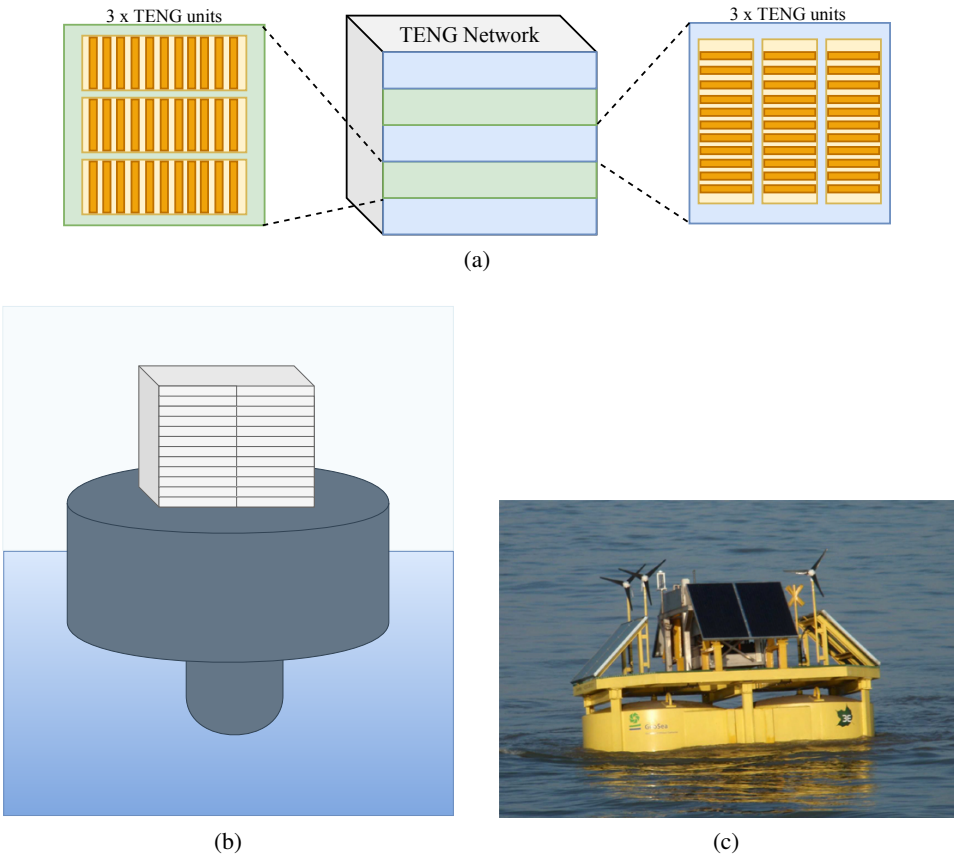

Figure 7.1: Propose of a TENG network where the (a) TENGs units are placed in different orientation attached to a (b) floating structure. (c) Flidar prototype as example (from [35]).

7.2 Future work

A future work of this dissertation would be the study of the behavior of materials obtained in this project, explaining the reason for the results obtained here, and search for the best materials and surface treatment that can increase the performance of each unit.

Another future work would be continuing the study and the experimental evaluation of the power management strategy here presented, which can be a new approach, never implemented in a TENG system.

Furthermore, an experimental evaluation in a real scenario should be carried out, with a network system constituted by several units, to evaluate the performance in realistic oceanic conditions.

Appendix A

Schematic of the impedance multiplier board

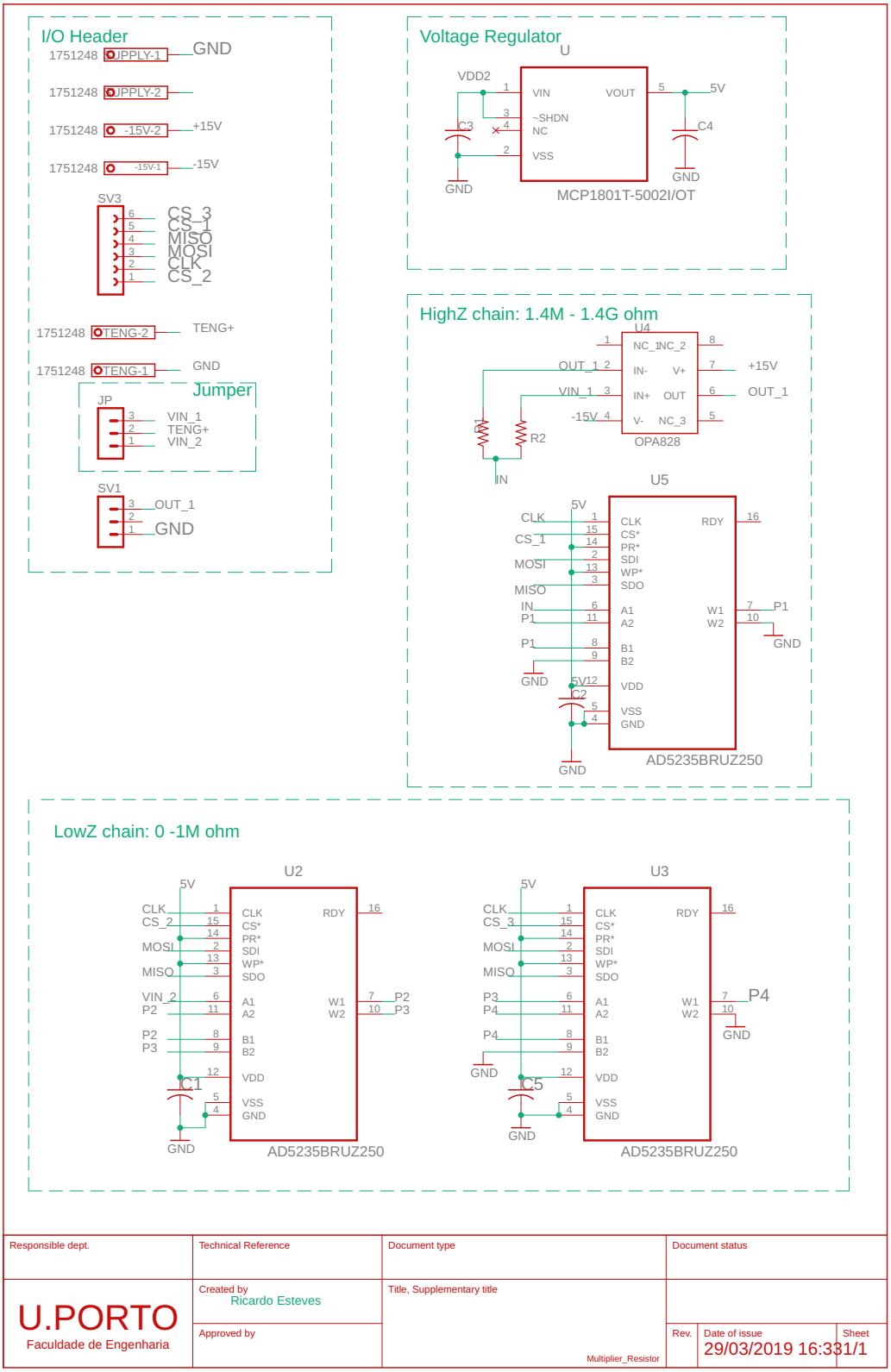

Responsible dept.	Technical Reference	Document type	Document status
U.PORTO Faculdade de Engenharia	Created by Ricardo Esteves Approved by	Title, Supplementary title Multiplier_Resistor	Rev. / Date of issue: 29/03/2019 16:33 / Sheet: 1/1

References

[1] Russell B. Wynn, Veerle A.I. Huvenne, Timothy P. Le Bas, Bramley J. Murton, Douglas P. Connelly, Brian J. Bett, Henry A. Ruhl, Kirsty J. Morris, Jeffrey Peakall, Daniel R. Parsons, Esther J. Sumner, Stephen E. Darby, Robert M. Dorrell, and James E. Hunt. Autonomous underwater vehicles (AUVs): Their past, present and future contributions to the advancement of marine geoscience. *Marine Geology*, 352:451 – 468, 2014. doi:https://doi.org/10.1016/j.margeo.2014.03.012.

[2] Giacomo Marani, Song K. Choi, and Junku Yuh. Underwater autonomous manipulation for intervention missions AUVs. *Ocean Engineering*, 36(1):15 – 23, 2009. doi:https://doi.org/10.1016/j.oceaneng.2008.08.007.

[3] Alex Raventós, Ana Brito e Melo, António F. de O. Falcão, António Sá da Costa, António Sarmento, Augusto Barata da Rocha, David Krohn, Frank Neumann, José Carlos Matos, Karl Christian Strømsem, Lara Ferreira, Luis A. Vega, Nuno Matos, Peter Scheijgrond, and Tiago Morais. *Offshore Renewable Energy Current Status-Future Perspectives for Portugal*. INEGI INSTITUTE OF MECHANICAL ENGINEERING AND INDUSTRIAL MANAGEMENT, inegi março edition, 2014.

[4] Rui Li, Ye Li, Yixin Zhao, Yinfeng Li, and Yu Li. Harvest of ocean energy by triboelectric generator technology. *Applied Physics Reviews*, 5(3), 2018. doi:10.1063/1.5008606.

[5] Zhong Lin Wang. Nano Energy Toward the blue energy dream by triboelectric nanogenerator networks. *Nano Energy*, 39(June):9–23, 2017. doi:10.1016/j.nanoen.2017.06.035.

[6] Feng Ru Fan, Zhong Qun Tian, and Zhong Lin Wang. Flexible triboelectric generator. *Nano Energy*, 1(2):328–334, 2012. doi:10.1016/j.nanoen.2012.01.004.

[7] Te-Chien Hou, Ya Yang, Hulin Zhang, Jun Chen, Lih-Juann Chen, and Zhong Lin Wang. Triboelectric nanogenerator built inside shoe insole for harvesting walking energy. *Nano Energy*, 2(5):856 – 862, 2013. doi:https://doi.org/10.1016/j.nanoen.2013.03.001.

[8] Zhong Lin Wang, Long Lin, Jun Chen, Simiao Niu, and Yunlong Zi. *Triboelectric Nanogenerators*. Springer, 2016. doi:10.1007/978-3-319-40039-6.

[9] Abdelsalam Ahmed, Zia Saadatnia, Islam Hassan, Yunlong Zi, Yi Xi, Xu He, Jean Zu, and Zhong Lin Wang. Self-Powered Wireless Sensor Node Enabled by a Duck-Shaped Triboelectric Nanogenerator for Harvesting Water Wave Energy. *Advanced Energy Materials*, 7(7), 2017. doi:10.1002/aenm.201601705.

[10] Xiaofeng Wang, Simiao Niu, Yajiang Yin, Fang Yi, Zheng You, and Zhong Lin Wang. Triboelectric Nanogenerator Based on Fully Enclosed Rolling Spherical Structure for Harvesting Low-Frequency Water Wave Energy. *Advanced Energy Materials*, 5(24):1–9, 2015. doi:10.1002/aenm.201501467.

[11] Minyi Xu, Tiancong Zhao, Chuan Wang, Steven L. Zhang, Zhou Li, Xinxiang Pan, and Zhong Wang. High power density tower-like triboelectric nanogenerator for harvesting arbitrary directional water wave energy. *ACS Nano*, 13, 01 2019. doi:10.1021/acsnano.8b08274.

[12] Jun Chen, Jin Yang, Zhaoling Li, Xing Fan, Yunlong Zi, Qingshen Jing, Hengyu Guo, Zhen Wen, Ken C Pradel, Simiao Niu, and Zhong Lin Wang. Networks of Triboelectric Nanogenerators for Harvesting Water Wave Energy: A Potential Approach toward Blue Energy. *ACS Nano*, 9(3):3324–3331, 2015. doi:10.1021/acsnano.5b00534.

[13] Ricardo Esteves, Cátia Rodrigues, João Ventura, André Pereira, Cândido Duarte, Vasco Correia, and Luís Pessoa. Experimental Evaluation of TENGs for Energy Harvesting in Maritime Applications. In *Proceedings of Oceans 2019, Marseille – Unpublished*. IEEE, June 2019.

[14] Simiao Niu and Zhong Lin Wang. Theoretical systems of triboelectric nanogenerators. *Nano Energy*, 14:161–192, 2014. doi:10.1016/j.nanoen.2014.11.034.

[15] Simiao Niu, Yu Sheng Zhou, Sihong Wang, Ying Liu, Long Lin, Yoshio Bando, and Zhong Lin Wang. Simulation method for optimizing the performance of an integrated triboelectric nanogenerator energy harvesting system. *Nano Energy*, 8:150–156, 2014. doi:10.1016/j.nanoen.2014.05.018.

[16] The Academic Faculty, Simiao Niu, and In Partial Fulfillment. *Theory of Triboelectric Nanogenerators for Self- Powered Systems Copyright © Simiao Niu 2016 Theory of Triboelectric Nanogenerators for Self-*. PhD thesis, Georgia Institute of Technology, 2016.

[17] Simiao Niu, Ying Liu, Sihong Wang, Long Lin, Yu Sheng Zhou, Youfan Hu, and Zhong Lin Wang. Theory of sliding-mode triboelectric nanogenerators. *Advanced Materials*, 25(43):6184–6193, 2013. doi:10.1002/adma.201302808.

[18] Simiao Niu, Ying Liu, Sihong Wang, Long Lin, Yu Sheng Zhou, Youfan Hu, and Zhong Lin Wang. Theoretical investigation and structural optimization of single-electrode triboelectric nanogenerators. *Advanced Functional Materials*, 24(22):3332–3340, 2014. doi:10.1002/adfm.201303799.

[19] Simiao Niu, Ying Liu, Xiangyu Chen, Sihong Wang, Yu Sheng, Long Lin, Yannan Xie, and Zhong Lin. Theory of freestanding triboelectric- layer-based nanogenerators. *Nano Energy*, 12:760–774, 2015. doi:10.1016/j.nanoen.2015.01.013.

[20] Zhao Xuejiao, Guang Zhu, Youjun Fan, Hua Yang Li, and Zhong Lin Wang. Triboelectric charging at the nanostructured solid/liquid interface for area-scalable wave energy conversion and its use in corrosion protection. *ACS nano*, 9, 07 2015. doi:10.1021/acsnano.5b03093.

[21] Qiongfeng Shi, Hao Wang, Han Wu, and Chengkuo Lee. Self-powered triboelectric nanogenerator buoy ball for applications ranging from environment monitoring to water wave energy farm. *Nano Energy*, 40:203 – 213, 2017. doi:https://doi.org/10.1016/j.nanoen.2017.08.018.

[22] Yunlong Zi, Simiao Niu, Jie Wang, Zhen Wen, Wei N. Tang, and Zhong Lin Wang. Standards and figure-of-merits for quantifying the performance of triboelectric nanogenerators. *Nature Communications*, 6(8376):1536–1539, Aug 2015. doi:10.1038/ncomms9376.

[23] Inc. Tektronix. *MDO3000 Series Mixed Domain Oscilloscopes User Manual*, 2014.

[24] Stanford Research Systems. *SR560 Manual - Low-Noise Voltage Preamplifier*, 2004.

[25] Application Note, High Impedance, Op Amps, and Literature Number. *Impedance Op Amps AN-241*.

[26] Keysight Technologies. *Keysight 34410A/11A 6 ½ Digit Multimeter*, 2014.

[27] Tektronix Inc. *MDO4000B, MDO4000, MSO4000B, DPO4000B and MDO3000 Series Oscilloscopes Programmer Manual*, 2013.

[28] Simiao Niu, Xiaofeng Wang, Fang yi, Yu Sheng Zhou, and Zhong Lin Wang. A universal self-charging system driven by random biomechanical energy for sustainable operation of mobile electronics. *Nature Communications*, 6:8975, 12 2015. doi:10.1038/ncomms9975.

[29] Fengben Xi, Yaokun Pang, Wei Li, Tao Jiang, Limin Zhang, Tong Guo, Guoxu Liu, Chi Zhang, and Zhong Lin Wang. Universal power management strategy for triboelectric nanogenerator. *Nano Energy*, 37:168 – 176, 2017. doi:https://doi.org/10.1016/j.nanoen.2017.05.027.

[30] Ronan Hinchet, Ali Ghaffarinejad, Yingxian Lu, Javad Yavand Hasani, Sang-Woo Kim, and Philippe Basset. Understanding and modeling of triboelectric-electret nanogenerator. *Nano Energy*, 47:401 – 409, 2018. doi:https://doi.org/10.1016/j.nanoen.2018.02.030.

[31] A. Zaky, M. Shehata, Y. Ismail, and H. Mostafa. Characterization and model validation of triboelectric nanogenerators using verilog-a. *IEEE*, pages 1536–1539, Aug 2017. doi:10.1109/MWSCAS.2017.8053228.

[32] Yunlong Zi, Jie Wang, Sihong Wang, Shengming Li, Zhen Wen, Hengyu Guo, and Zhong Lin Wang. Effective energy storage from a triboelectric nanogenerator. *Nature Communications*, 7:10987, 03 2016. doi:10.1038/ncomms10987.

[33] Xiaoliang Cheng, Liming Miao, Yu Song, Zongming Su, Haotian Chen, Xuexian Chen, Jinxin Zhang, and Haixia Zhang. High efficiency power management and charge boosting strategy for a triboelectric nanogenerator. *Nano Energy*, 38:438 – 446, 2017. doi:https://doi.org/10.1016/j.nanoen.2017.05.063.

[34] Haruo Kobayashi and Takashi Nabeshima. *Handbook of Power Management Circuits*. panstanford, 2016. doi:https://doi.org/10.1201/b19357.

[35] Julia Gottschall, Brian Gribben, Detlef Stein, and Ines Würth. Floating lidar as an advanced offshore wind speed measurement technique: Current technology status and gap analysis in regard to full maturity. *Wiley Interdisciplinary Reviews: Energy and Environment*, 6, 05 2017. doi:10.1002/wene.250.